

# **Integrated Thermal Systems and Controls Modelling for AUTO Mode Simulation and Optimization**

By

**Mingzhe Chang**

A Thesis  
Submitted to the Faculty of Graduate Studies  
through the Department of Mechanical, Automotive & Materials Engineering  
in Partial Fulfillment of the Requirements for  
the Degree of Master of Applied Science  
at the University of Windsor

Windsor, Ontario, Canada

2020

© 2020 Mingzhe Chang

# **Integrated Thermal Systems and Controls Modelling for AUTO Mode Simulation and Optimization**

By

**Mingzhe Chang**

APPROVED BY

---

N. Van Engelen  
Department of Civil and Environmental Engineering

---

M. Ahamed  
Department of Mechanical, Automotive & Materials Engineering

---

O. Jianu, Advisor  
Department of Mechanical, Automotive & Materials Engineering

September 8<sup>th</sup>, 2020

# Declaration of Originality

I hereby certify that I am the sole author of this thesis and that no part of this thesis has been published or submitted for publication.

I certify that, to the best of my knowledge, my thesis does not infringe upon anyone's copyright nor violate any proprietary rights and that any ideas, techniques, quotations, or any other material from the work of other people included in my thesis, published or otherwise, are fully acknowledged in accordance with the standard referencing practices. Furthermore, to the extent that I have included copyrighted material that surpasses the bounds of fair dealing within the meaning of the Canada Copyright Act, I certify that I have obtained a written permission from the copyright owner(s) to include such material(s) in my thesis and have included copies of such copyright clearances to my appendix.

I declare that this is a true copy of my thesis, including any final revisions, as approved by my thesis committee and the Graduate Studies office, and that this thesis has not been submitted for a higher degree to any other University or Institution.

# Abstract

Virtual product development has become the preferred approach for vehicle A/C system development. The advantages provided by virtual modelling compared to traditional approach are accelerated development pace and reduced cost. The thesis focuses on virtual modelling of the A/C system on a SUV vehicle based on experimental data.

A virtual model of the A/C system is constructed and calibrated in Simcenter Amesim. The model includes a vapour-compression refrigeration cycle and a cabin air model. The components are modelled and calibrated based on supplier data. The two thermal systems interact thermally at the evaporator level. The cabin air blower unit with a PI controller and a small DC motor is also modelled in MATLAB/Simulink.

The virtual thermal model is able to simulate the cabin air temperature development during High Ambient AUTO mode drive cycle. The controlled DC motor system tracks reference speed to provide adequate air flow for the cabin. The virtual models can be used for A/C system and components performance analysis and optimization. The modelling process provides deeper understanding on thermal and control systems design.

# Acknowledgements

The two-year Dual International Masters Degree program comes to an end with the completion of the thesis. It was a great learning opportunity and a truly unique experience. I would like to express my gratitude to all the people and organizations who had been involved in this journey. My achievement is not possible without all of your support.

I would first like to thank my academic advisor, Dr. Ofelia A. Jianu, who has always been there to support me and help me navigate through the “swamps” during academic research. I wouldn’t be where I am today without her guidance along the way.

I would also like to thank the product development team from FCA Canada, especially Shankar Natarajan and Yasaman Masoudi, who provided valuable training and advice towards the technical aspect of my thesis. I learned a lot about product development in the automotive industry.

Special thanks to all project coordinators: Dr. Jennifer Johrendt from University of Windsor, Marie Mills from FCA Canada and Dr. Giovanni Belingardi from Politecnico di Torino. This year’s COVID-19 situation has brought great uncertainties to the last part of the program, and I appreciate everything they did to help arrange the students to come back to Canada.

I would like to thank my committee members Dr. N. Van Engelen and Dr. M. Ahamed for taking the time and attention to review my work. The feedback during proposal provides tremendous value for improvement.

Lastly, I would like to express special thanks to my wife, Fangfei, for her unconditioned love and support during the journey of my graduate studies. Her prayers for the success of this small family must have been answered.

# Contents

<b>Declaration of Originality</b>	<b>III</b>
<b>Abstract</b>	<b>IV</b>
<b>Acknowledgements</b>	<b>V</b>
<b>List of Tables</b>	<b>IX</b>
<b>List of Figures</b>	<b>XI</b>
<b>List of Abbreviations</b>	<b>XII</b>
<b>Nomenclature</b>	<b>XIII</b>
<b>1 Introduction</b>	<b>1</b>
1.1 Background . . . . .	1
1.2 Objectives . . . . .	2
1.3 Thesis Outline . . . . .	2
<b>2 Literature Review</b>	<b>4</b>
2.1 Thermal Systems Modelling . . . . .	5
2.1.1 One-dimensional Approach . . . . .	5
2.1.2 Three-dimensional Approach . . . . .	5
2.1.3 Multi-zone Cabin . . . . .	6
2.1.4 Systems with Multi-evaporator and Multi-row Air Ducts . . . . .	6
2.1.5 Thermal Loads . . . . .	7
2.1.6 Thermal Comfort Model . . . . .	8
2.2 Control Design . . . . .	9
2.2.1 System Identification . . . . .	9
2.2.2 PID Controller . . . . .	11

2.2.3	Model Predictive Control (MPC) . . . . .	13
2.2.4	Fuzzy Control . . . . .	13
<b>3</b>	<b>Thermal Systems Modelling</b>	<b>15</b>
3.1	A/C Refrigerant Loop . . . . .	16
3.1.1	Compressor . . . . .	19
3.1.2	Condenser . . . . .	21
3.1.3	Evaporator . . . . .	26
3.1.4	Internal Heat Exchanger (IHX) . . . . .	28
3.1.5	Thermal Expansion Valve (TXV) . . . . .	29
3.2	Drive Cycles . . . . .	32
3.3	Cabin Air Model . . . . .	33
3.3.1	Thermal Mass . . . . .	34
3.3.2	External Heat Transfer . . . . .	34
3.3.3	Internal Heat Transfer . . . . .	35
3.3.4	Hot-soak and Cool-down . . . . .	38
<b>4</b>	<b>Control Design</b>	<b>39</b>
4.1	Methodology . . . . .	39
4.2	DC Motor Assembly . . . . .	40
4.2.1	Linear System Analysis . . . . .	40
4.2.2	Brushless DC Motor . . . . .	43
4.2.3	Three-Phase Inverter . . . . .	45
4.2.4	Hall Effect Sensor . . . . .	47
4.2.5	Commutation Logic . . . . .	47
4.2.6	PWM Duty Cycle . . . . .	49
4.2.7	Blower Fan . . . . .	51
4.3	DC Motor Controller . . . . .	53
4.3.1	Tuning Rules . . . . .	56
4.3.2	Discrete Time Domain . . . . .	57
4.3.3	Numerical Solver . . . . .	58
<b>5</b>	<b>Results and Discussion</b>	<b>60</b>
5.1	Thermal Systems Performance . . . . .	60
5.1.1	A/C Refrigerant Loop . . . . .	60
5.1.2	Cabin Air Model . . . . .	62
5.2	DC Motor Performance . . . . .	63

<b>6 Conclusion and Future Work</b>	<b>66</b>
6.1 Future Work . . . . .	66
<b>Bibliography</b>	<b>73</b>
<b>Appendix</b>	<b>74</b>
.1 MATLAB scripts for linear system analysis . . . . .	74
<b>Vita Auctoris</b>	<b>77</b>

# List of Tables

- 4.1 DC motor parameters . . . . . 41
- 4.2 BLDC motor parameters . . . . . 45
- 4.3 Ziegler-Nichols: Ultimate Gain Method . . . . . 56
- 4.4 Ziegler-Nichols: Reaction Curve Method . . . . . 57

# List of Figures

3.1	P-h diagram of a non-ideal vapour-compression refrigeration cycle [1] . . .	17
3.2	A/C refrigerant loop in Simcenter Amesim [2] . . . . .	18
3.3	Compressor volumetric efficiency 3D look-up table. . . . .	21
3.4	Compressor isentropic efficiency 3D look-up table. . . . .	21
3.5	Condenser in Simcenter Amesim . . . . .	22
3.6	Condenser temperature 4D look-up table at a fixed vehicle speed . . . . .	23
3.7	Condenser calibration . . . . .	26
3.8	Evaporator calibration . . . . .	27
3.9	Internal heat exchanger detailed view . . . . .	29
3.10	The thermal expansion valve component in Amesim . . . . .	30
3.11	Four-dimension diagram for the thermal expansion valve [2] . . . . .	31
3.12	Schematic view of vehicle cabin model in Amesim . . . . .	36
3.13	Air gap inside the door . . . . .	37
4.1	Block diagram of a DC motor' transfer function . . . . .	41
4.2	Step response of a DC motor . . . . .	43
4.3	DC motor subsystem in Simulink . . . . .	44
4.4	Block diagram for three-phase inverter . . . . .	46
4.5	A pair of coils is polarized by three-phase inverter [3] . . . . .	46
4.6	Back EMF profiles with different pole pairs . . . . .	47
4.7	Block diagram for Hall effect sensor . . . . .	48
4.8	Commutation logic table . . . . .	48
4.9	pulse-width modulation (PWM) generator with two logic tables and a switch	50
4.10	PWM duty cycle profile . . . . .	51
4.11	Fan speed (rpm) as a function of air flow rate (SCFM) . . . . .	52
4.12	Derived fan speed profile for High Ambient AUTO mode drive cycle . . . . .	52
4.13	Closed-loop block diagram for DC motor control . . . . .	53
4.14	DC motor response with P controller . . . . .	54

4.15	DC motor response with proportional-integral (PI) controller . . . . .	55
5.1	Evaporator outlet air temperate . . . . .	61
5.2	Compressor discharge pressure . . . . .	62
5.3	Cabin air temperate . . . . .	63
5.4	DC motor's speed tracking performance and controller's voltage command .	64
5.5	DC motor's speed and reference speed (scaled down by 100x) . . . . .	65

# List of Abbreviations

- 1D** One-dimensional. 4–7, 16, 33, 38, 66
- BLDC** brushless DC motor. 2, 3, 44–47, 49, 51–53, 57, 64
- CFD** Computational Fluid Dynamics. 5, 6
- FPC** Fiala Physiological Comfort. 8
- GWP** global warming potential. 16
- HEX** heat exchanger. 16, 17
- IHX** internal heat exchanger. 16, 17, 28, 29, 61
- LQR** linear–quadratic regulator. 12
- LTI** linear time-invariant. 10
- MPC** Model Predictive Control. 3, 13, 14
- PI** proportional-integral. XI, 3, 12, 55, 57, 64
- PID** proportional-integral-derivative. 2, 3, 9, 11–14, 39, 40, 53, 54, 56, 57
- PMV** Predicted Mean Vote. 8, 13, 14
- PPD** Predicted Percentage of Dissatisfied. 8
- PWM** pulse-width modulation. X, 3, 39, 40, 43, 44, 49–51, 53
- TXV** thermal expansion valve. 7, 15–17, 28–31

# Nomenclature

$\alpha$  Absorptivity. 33, 35

$\epsilon$  Emissivity. 35

$\rho$  Reflectivity. 33, 35

$\tau$  Transmissivity. 33, 35

Nu Nusselt number. 24, 25, 37

$a$  Nusselt number constant a. 24

$b$  Nusselt number constant c. 24

$c$  Nusselt number constant c. 24

Pr Prandtl number. 24

Re Reynolds number. 24

$C_d$  Hydraulic diameter. 24, 25

$C_p$  Specific heat. 25

$\mu$  Dynamic viscosity. 24

$\nu$  Kinematic viscosity. 25

# Chapter 1

## Introduction

### 1.1 Background

Vehicle A/C system development has traditionally been an iterative process in which the engineers design the system, build the prototype, perform physical test and revise the design based on the actual performance. The development iteration continues until the performance satisfies the design goal. By performing physical experiments, the results are highly reliable and can be used to improve the design. However, the traditional approach faces massive cost associated with conducting physical tests and it also suffers from slow development pace. The automotive industry is in search of alternative ways to address these problems.

In recent decades, virtual product development has gained popularity due to more powerful computers and matured simulation software solutions as it addresses the two shortcomings of traditional development process by reducing the need to conduct physical tests and accelerating the pace of the development. Hence, the need for prototyping has been greatly reduced as the virtual model can provide accurate simulation result. In addition, virtual modelling shows great flexibility in areas where the design is open and faces uncertainties.

Vehicle A/C system development benefits from virtual product development approach. The components and structure can be constructed as a virtual model in the software, while the thermal interactions between different closed-loop systems can be simulated. The automatic control algorithm adds extra complexity but it can be analyzed and developed in the software as well. Moreover, due to an increasing number of drive cycle tests for a new vehicle to fulfill during development stage, virtual modelling shows great advantage and flexibility in areas where the engineers have to prepare the system for drive cycle tests. System performance and minor design changes can be obtained from simulation directly. Consequently, virtual modelling is the popular choice for A/C system development.

## 1.2 Objectives

A virtual software model for the automatic A/C system on a mid-size SUV vehicle is going to be constructed and validated against experimental data. The complete software model consists of a vapour-compression refrigeration cycle referred to as “A/C refrigerant loop” throughout the thesis, and a vehicle cabin air model. In addition, the cabin air blower assembly including a DC motor and a proportional-integral-derivative (PID) type controller is also constructed as a standalone system.

Virtually modelling an A/C system requires the understanding of the working principle of each component and how to integrate them together. Fundamental knowledge on heat transfer mechanisms and control logic is also a must for dealing with thermal models and DC motor control. To develop a virtual model to simulate the A/C system performance on the SUV vehicle, the following objectives are met as a result of this research:

- Develop an A/C refrigerant loop. Major components including compressor, condenser, evaporator and thermal expansion valve are built and calibrated against supplier data. The system undergoes refrigerant charge initialization process to ensure the performance follows the physical system during drive cycle test.
- Obtain the cabin air model. The cabin air model is approached based on the calibrated refrigerant loop that supplies cool air. Heat interactions between thermal mass and cabin air are carefully modelled based on the knowledge of external heat load and cabin geometries.
- Select a controller such that the blower can be controlled and output the desired amount of air in the cabin. A brushless DC motor (BLDC) motor is implemented in MATLAB/Simulink. The closed-loop control system with a PID type controller is modelled and tuned. The system is designed to suit automotive applications with integration in mind.

In summary, the goal is to develop a virtual A/C system model that is able to provide satisfactory simulation results for drive cycle test. Ideally, the blower assembly will be integrated to the thermal system to achieve automatic temperature control to fully simulate the working of automatic A/C system.

## 1.3 Thesis Outline

The thesis begins with a literature review on the methodologies of building one-dimensional thermal systems. Various related topics are explored including thermal load calculation,

multi-zone cabin and 3D approach. The second part of literature review focuses on control system design. The main features and applications of PID controller, Model Predictive Control (MPC) controller and fuzzy logic control are discussed.

In Chapter 3, the details on how to build and calibrate each component in A/C refrigerant loop are laid out, followed by refrigerant charge initialization process. Similar building procedures also apply to cabin air model. Finally, the two systems are connected and validated against experimental data.

Chapter 4 turns the focus to modelling the blower motor assembly. A closed-loop control system with a PI controller and a PWM driven BLDC motor are built and tuned. The result is a controlled blower assembly that is able to track the reference air flow rate supplied to the cabin.

Simulation results and discussion about the results for both thermal and control systems are presented in Chapter 5. Lastly, a summary of accomplishments and comments on future improvements together make up Chapter 6.

# Chapter 2

## Literature Review

The primary focus of this research is to simulate the vehicle A/C system during AUTO mode operation. The literature review therefore consists of two parts: thermal systems modelling and control logic (controller design and integration with thermal systems). This structure represents the steps took in the research process.

Thermal systems are the building blocks of the research and thus they have to be built and calibrated first. There are mainly two approaches for modelling thermal systems: One-dimensional (1D) and three-dimensional (3D); both of them have pros and cons with respect to model complexity, computation accuracy and speed. For certain systems such as refrigerant loop, 1D modelling gives satisfactory results on refrigerant mass flow rate and temperature. More complex systems (e.g., cabin air loop) may benefit from 3D modelling as it involves temperature distribution inside the cabin; another approach is to have the cabin volume divided into multiple 1D zones to improve accuracy while still retaining a reasonable modelling effort.

Different types of control logic and controllers are then researched and compared. Special attention is paid to the input and output parameters of the controllers along with other constraints of the system in the literature. The methodology and implementation details for the integration of the controller and thermal systems is looked at. Lastly, the documentation of the two software tools used during the research (Simcenter Amesim and MATLAB/Simulink) is studied and referenced.

Related topics are also explored, including but not limited to thermal load calculation, human flux model and advanced control methods such as fuzzy control law. Due to the scope of the research and author's limited technical capabilities, it is not possible to implement all of said topics in the research work. Nonetheless, exploring the diverse possibilities serves as an important stage in the research as it provides inspirations.

## **2.1 Thermal Systems Modelling**

### **2.1.1 One-dimensional Approach**

The basic methodology and workflow for 1D modelling and testing of A/C system at component and system level is demonstrated by Natarajan et al [4]. The vehicle cabin 1D model is represented by a moist-air volume with heat load entering through semi-transparent surfaces. During the simulation of the refrigerant loop, input conditions include compressor speed, condenser and evaporators inlet air conditions whereas output conditions include evaporators outlet air temperatures, compressor discharge pressure and head pressure. When the A/C system is operating in re-circulation mode, it is necessary to model the vehicle cabin, as the evaporator inlet air conditions depend on the heat transfer into the cabin. Heat load enters the cabin by radiation through transparent and opaque surfaces, forced convection, and conduction through surface materials; thermal interactions happening inside the cabin mainly are internal convection and conduction among interior materials. The amount of thermal mass inside the cabin is crucial in determining the cool-down temperature curve. The limitation of 1D model is that it can only predict one average temperature inside the cabin. Individual A/C system components are calibrated with supplier given geometry and performance data. The physical test is carried out on a SUV equipped with a dual A/C system in a wind tunnel; the results correlate well with 1D simulation results. The paper [4] provides insights into building a 1D model, i.e., implementing individual components into a 1D model and controlling input parameters. The virtual modelling process is achieved by using Simcenter Amesim [2] software.

Kiss and Lustbader [5] implemented 1D model of vehicle A/C system in MATLAB Simulink. In a similar approach, the 1D model consists of components of refrigerant loop and vehicle cabin. To improve computational time while still retaining certain level of accuracy, the fully-detailed model is simplified by altering S-functions in Simulink for the zero-dimensional (0D) volume and 1D pipe blocks. The results of steady-state operation and drive cycle based efficiency of the simplified models are adequately acceptable; the speed improvement is on the order of 10 and 100 fold, respectively.

### **2.1.2 Three-dimensional Approach**

The limitation of relying solely on 1D modelling is the lack of knowledge on temperature distribution inside the vehicle cabin. Research has been done to explore the possibility of combining 3D modelling method, i.e., Computational Fluid Dynamics (CFD), with traditional 1D modelling [6]. The author explains how to couple ANSYS® Fluent CFD solver

with 1D system model to better predict and visualize overall temperature distribution inside the bulk of vehicle cabin. While the 1D model is only capable of predicting one average temperature, the added 3D CFD solver can predict the temperature distribution in the cabin volume. Bhambare et al. [7] performed a 3D transient analysis of the climate inside a vehicle cabin. Two solvers, a Lattice-Boltzmann method based flow solver for convection heat transfer and a finite difference based solver for conduction and radiation, are coupled to achieve a good balance between the solution accuracy and simulation time. The cool-down simulation is validated by the wind tunnel test and shows good agreement. Pathuri et al. [8] divided the cabin air volume into 36 zones based on detailed geometric data and performed air flow analysis using 3D CFD solver; transient thermal behaviours of ducts and internal masses are also modelled. Good correlation between simulation and experimental data measured at vehicle level is achieved.

### **2.1.3 Multi-zone Cabin**

Due to enormous computational effort and complex modelling process required by CFD, it is not feasible to completely replace 1D modelling in the development stage of car A/C system with 3D modelling. A practical approach to bridge the gap between the two is to split the 3D model into multiple zones and solve for each zone using 1D modelling. Each zone provides the average air condition in its corresponding volume, hence the more zones there are, the more detailed and local information can be obtained about the whole vehicle cabin. Studies [8–10] show that 1D based multi-zone approach is a relatively good mid point between 1D and 3D modelling, providing relatively good results while not requiring extensive set-up and intensive computing resources. The zone-splitting strategy can either be based on vertical space (e.g., from top to bottom) or horizontal space if rear row air ducts are present; it is also possible to be based on individual occupant if finer temperature control is the goal. The implementation details of 1D multi-zone approach vary from project to project, based on their design priorities.

### **2.1.4 Systems with Multi-evaporator and Multi-row Air Ducts**

Multi-row air ducts A/C systems are often found in mid to large-sized vehicles, such as SUV and minivans. In most cases, a rear evaporator is required to drive the additional air ducts [8, 10, 11]. The purpose of such a large and complex system is to effectively and uniformly control cabin air climate. Multi-zone becomes a quite handy analysis approach in these kind of applications. The vehicle platform for this research has a single-evaporator and single-duct configuration. However, leaving the possibility for the software model to

expand in the future to incorporate multi-evaporator and multi row ducts configurations still seems valuable. Muthusamy et al. [10] built a 1D analysis platform for a large vehicle with two evaporators and three air ducts rows. The cabin is essentially split into three zones corresponding to the front, middle and rear rows. Air flow from the rear evaporator is split into the middle and rear rows, based on a split ratio estimated by comparing local thermal loads. Andrès et al. [11] explored the possibility of fitting a traditional multi-evaporator A/C system into an electrical vehicle. They added an additional evaporator as a chiller to cool the batteries as well as replace the thermal expansion valve (TXV) with an electronic expansion valves (EXV). The dynamic coupling of multiple evaporators with thermal expansion devices prove to be challenging with respect to rejecting step disturbances. The potential solution is to introduce more advanced control strategies to regulate the electronic expansion valves.

### **2.1.5 Thermal Loads**

Thermal loads that are imposed to the vehicle cabin are one of the most important factors that need to be accurately estimated. The process involves taking consideration of thermal sources and building heat transfer models for different materials. Zheng et al. [12] suggest a simple method to calculate vehicle heat load. Various heat load sources including solar radiation, seal-infiltration, occupants and blower motor are separately calculated and summed up; the result is validated by wind tunnel tests. Fayazbakhsh and Bahrami [13] develop mathematical models to calculate heating and cooling load from major sources. The models take vehicle geometry, material properties and driving condition characteristics as input and calculates the thermal loads by different sources for the simulation in real time. The results show that radiation and ventilation load, i.e. the ambient air entering and cabin air leaving, play important roles in cabin temperature variation. Sanaye and Dehghandokht [14] take a similar approach to predict vehicle cabin temperature by performing mass and energy conservation analysis. A new parameter, air circulation ratio, is defined in addition to solar load, ventilation load and evaporator capacity. Furthermore, the authors performed a parametric analysis, which is based on vehicle speed, number of occupants and A/C mass flow rate to study the effect of each parameter on the cabin temperature. Rugh et al. [15] proved that solar control PVB glass can improve fuel economy by reducing A/C power consumption. Two identical vehicles with different glasses were tested under the sunlight. Vehicle cabin model was simplified by considering cabin air and mass only, omitting the occupant thermal comfort model. Thermal analysis on hot soak and cool down tests show potentially 4% reduction in A/C power by setting a lower vent temperature.

### 2.1.6 Thermal Comfort Model

One of the most important goals of the vehicle A/C system is to let the occupants feel comfortable, both physiologically and psychologically. Thermal comfort level serves as an additional criterion to determine the overall performance of the A/C system during product development phase. On the other hand, thermal comfort level is not a parameter that can be easily determined in a mathematical way since it involves a large amount of factors and is highly subjective. Environmental factors that may have an effect on thermal comfort level include air temperature, air velocity, relative humidity and radiant heat [16]. According to the same study, the other set of factors, which are more personal to the occupants, include but not limited to activity level and clothing insulation.

The studies around thermal comfort of occupants inside a vehicle cabin are largely based on two parameters: Fanger's Predicted Mean Vote (PMV) and Predicted Percentage of Dissatisfied (PPD) [17]. The PMV predicts the average thermal sensation felt by a large group of people exposed to the same environment; the index ranges from -3 (cold) to +3 (hot) with 0 being neutral. As an average agreement on the thermal discomfort level, however, the individual outlier data is underrepresented; therefore, the PMV index alone is not sufficient to define how uncomfortable the occupants are. The PPD is then introduced by Fanger. It is a quantitative prediction of percentage of thermally dissatisfied people based on the PMV, addressing the outlier data that may be underrepresented in the calculation of PMV. The two indexes are often employed together to determine the overall thermal comfort of occupants.

The aforementioned Fanger's indexes were originally developed in 1970s. Subsequent human flux models were built based on Fanger's indexes. The Fiala Physiological Comfort (FPC) model [18] is a mathematical model that is capable of not only predicting thermal sensation and comfort based on physiological effects, but also simulating heat and moisture dissipation from human body. Therefore, it is an active model that can simulate the thermal interactions between the occupants and the cabin environment. Lorenz et al. [19] explore the effects of thermal interactions with the occupants using the FPC model. The conclusion is that auxiliary thermal devices such as seat heating and low emissivity window glass could reduce the heating energy demand and enhance thermal comfort during code environment.

Auxiliary thermal devices often have a positive contribution to the thermal comfort of occupants while not requiring excessive energy to operate. Kubota et al. [20] modelled auxiliary thermal devices such as air-conditioned seat and heated steering wheel and incorporated them into the vehicle cabin model. The local thermal comfort level is estimated based on heat loss of occupants; an equivalent temperature  $T_{eq}$  is calculated and validated against declared values of test subjects.

## 2.2 Control Design

The design and implementation of control logic dictates the behaviour of the automatic A/C system in real world operations within the physical limit. The works of automotive A/C system can be seen as an analogy for works of human body: the thermal systems behave as the “body” while the control logic functions as the “brain” by taking information from sensors as input, processing them and issuing commands to physical hardware. Optimized control logic strikes the balance between the performance of the hardware and the energy consumption rate. In other words, it helps the A/C system to achieve reasonable thermal comfort in an economical way.

Controllers with different types of control logic can be applied to vehicle A/C application. There are three types of control methods that are going to be explored in this chapter: traditional feedback control, predictive control and fuzzy control. Feedback control is widely adopted in many industry applications usually in the form of a PID controller. Feedback controller is easy to build and tune while also able to provide good performance. Predictive control, or feed-forward control, used to be rare due to high computational resource requirement, but is becoming increasingly popular these days with more capable on-board computer chips [21]. Fuzzy control is on the contrary to classical control, as it analyzes input signal in terms of logical variables that take on continuous values between 0 and 1. Fuzzy logic is closer to human logic, making it possible to use human experience can be used to design the controller [22].

Different design approaches are reviewed in the following sections. The methodology for the integration between thermal systems and controller is researched and summarized. It is vital to understand how different systems work together in the context of virtual product development. However, due to the vast number of software platforms used in different research, the focus is on general idea rather than technical details.

### 2.2.1 System Identification

The first step towards building a control solution is to obtain the mathematical model of the plant or physical process that is going to be controlled. Ideally the model can be derived analytically based on the first principle (Newton’s equations). In this case, the model is called a white-box model as its physical process is perfectly transparent. However, in practical applications, it is often too complex or impossible to obtain a white-box model. Another way to obtain the model is by going through system identification: observe the behaviour (output) of the physical system and try to determine a mathematical description of the model. If the system is completely unknown and only the output can be observed,

it is referred to as a black-box model [23]. A grey-box model, also called a hybrid model, consists of a combination of first principle (white-box) and empirical (black-box) components [24]. System identification techniques exist to help determine the model of a plant when it is not available as a white-box model.

A comprehensive review on system identification, particularly on nonlinear black-box modelling techniques are prepared by Sjöberg et al. [25]. Nonlinear black-box modelling is considered difficult to tackle due to the fact that nothing from a wide spectrum of possible model descriptions can be excluded. The fundamentals of the black-box modelling can be seen as two mapping processes: the first mapping is from observed data to a regression vector; the second mapping is by a nonlinear, function expansion type, to the space of the system's outputs. The state-space regressors are less restricted in their internal structure than the input-output regressors, hence it might be possible to obtain a more efficient model with a smaller number of regressors. A general recommendation is to start by carefully observing the data and the physics of the system, and work the way from simple linear model to nonlinear model only if absolutely necessary. Lastly, validate the model against fresh data which were not used for identification.

Romijn et al. [26] claim that many model reduction techniques for high-order nonlinear dynamic system fail to reduce computational effort, despite that fact that the order of a model is significantly reduced. By treating the entire system as a black-box and performing system identification and reduction, the favourable structure of the original model is lost. The authors propose a grey-box approach by separating the white-box and black-box components of the model, performing reduction individually and re-coupling together. Proper orthogonal decomposition (POD) is used for an efficient reduction of large-scale linear and nonlinear systems. As a result, a reduced grey-box model with less nonlinear complexity is obtained. This novel technique is applied to obtain a heat convection-conduction model. The combined model perform reasonably well compared to a black-box model.

The plant models for vapour compression refrigeration cycle and indoor dynamics are analytically derived by Lin and Yeh [27] using bond-graph approach [25]. The two plant models are subsequently identified and reduced into a single linear time-invariant (LTI) system with two inputs (compressor speed, expansion valve opening angle) and three outputs (evaporator temperature, superheat temperature and condenser temperature). The model parameters are found out by conducting physical experiments and using least-square method. The caveat is that the system is identified at a fixed operating condition with only inputs perturbed by square waves. Furthermore, the model is validated against the same set of data which does not align with the recommendation by Sjöberg et al. [25]. This may not be an important issue as indoor A/C systems usually operate in fixed conditions.

### 2.2.2 PID Controller

One of the most widely adopted controller designs based on feedback control principle is PID controller. The output sum of proportional, integral and derivative terms offer treatment for both steady-state and transient response of the controlled system.

Bansal et al. [28] reviewed a large number of PID controller tuning techniques. There are classical heuristic techniques such as Ziegler-Nichol [29] and Cohen-Coon as well as optimization and adaptive techniques. The authors concluded that classical techniques require less computing effort and are simple to implement. However, due to the initial assumptions made about the plant and the desired output, the controller often needs to be further tuned for desired results. Optimization techniques involve a cost function that needs to be minimized in order to balance tracking error and command activity. Adaptive techniques were also presented, with the basic principle being that the controller gains are found under different operating conditions and are handled by gain scheduling [28].

Li et al. [30] addressed difficulties on the tuning of integral and derivative terms. The nonlinear median filter was recommended over the low pass filter in removing impulse spikes of derivative action caused by a sudden change of disturbance. Several integral wind-up remedies were briefly discussed. The authors also presented a computerized, simulation-based approach to illustrate the design results for first-order, higher order and nonlinear plants.

Integral windup is the result of PID controller command activity not being achieved due to actuator saturation [31]. Since the PID controller relies on the fact that the command activity are fully applied, its integrator parameter is adjusted aggressively, resulting in oscillation and poor reference tracking. The concept of integrator wind up is explained by Bohn and Atherton [31] and several PID anti wind-up strategies included in early version of MATLAB/Simulink are explored and compared.

A strategy that works well in continuous-time domain may suffer difficulties in discrete-time domain. Scottedward Hodel and Hall [32] studied the behaviours of common anti wind-up strategies in both continuous and discrete-time domains. The problem with clamping or freezing the integrator value is that there is no guarantee that the control signal will come out of saturation soon or at all. Additional feedback action that provides error tracking helps in continuous-time domain. For discrete-time domain, a switch mechanism is introduced by the two authors that linearly adjusts the integrator to reduce the saturation based on feedback error term.

Although PID controller is applicable to many applications and often provide satisfactory results with basic tuning, it does not generally provide optimal control, whereas a cost function of the plant process is being minimized and hence the performance can be opti-

mized. The fundamental problem is that the feedback loop, with constant gain parameters, does not have direct knowledge on the plant process. Therefore, PID controller alone is passive and the performance can be poor in some applications.

To improve reference tracking performance, Visioli [33] proposed a new design where a nonlinear feed-forward action is added to the PID controller. The feed-forward action generates a user-defined transition time constant when a set-point change is present. The time constant handles the trade-off between performance, command activity and robustness. The integral and derivative parameters were tuned in order to reject disturbance. With a step input as reference signal and a first-order plus dead time (FOPDT) plant model, the new design shortened the settling time compared to a PID controller without feed-forward action.

In practical applications, PID controllers often need to take discrete-time data sets as input. It is important to adapt continuous-time domain controllers to be used in discrete-time domain and ensure the stability of the resulting control system. Mizumono et al. [34] built an adaptive PID controller based on almost strictly positive real (ASPR) property of the controlled system for discrete-time systems, so the asymptotic stability of the resulting adaptive control system can be guaranteed. To deal with causality problems brought by ASPR property in discrete-time domain system, a parallel feed-forward compensator (PFC) design was employed to ensure robustness. The effectiveness of the design was validated against water level control SISO system.

A systematic approach to build PI controllers for an indoor A/C system was demonstrated by Lin and Yeh [27]. Both the vapour compression refrigeration cycle and the indoor dynamics models are identified and linearized. A group of PI controllers with cascading structure is responsible for regulating the compressor speed and thermal expansion valve opening angle to satisfy the set temperatures for evaporator and condenser. The design of PI controllers was based on linear-quadratic regulator (LQR) methodology and the tuning of anti-windup compensator is largely based on trail-and-error. The requirement was to have a good transient response on the indoor temperature while also maintaining zero overshoot. Subsequent study by Yeh et al. [35] added indoor and outdoor fans to the existing plant models. The input of the system consisted either the indoor or the outdoor fan speed, and one more PI controller for the actuator of the fan. The authors concluded that adding the outdoor fan will improve steady state power efficiency and the indoor fan will improve transient response.

### 2.2.3 Model Predictive Control (MPC)

Mařík et al. [36] focused on intelligent control of commercial building HVAC system. Traditional rule-based control strategies and Model-based Predictive Control (MPC), along with thermal performance monitoring technique are compared and discussed. The generic mathematical model for MPC is laid out and explained. The conclusion is that rule-based control strategies are generally only capable of finding a sub-optimal solution, although much more sophisticated implementations exist; model-based predictive control are more complex but are able to provide better HVAC efficiency.

Within the field of MPC controllers, there are linear and non-linear variants, which are described in the following paragraphs.

Conventional feedback control tries to correct errors based on signal feedback from the plant output without knowing the presence of disturbances, inevitably introducing phase delay to A/C control system. Lim et al. [37] addressed this issue by developing a linear MPC algorithm and tested it on a virtual vehicle model. The proposed predictive control predicts the behaviour of disturbances in advance and then optimizes the compressor speed.

MATLAB/Simulink is often used for controller design and tuning. Wang et al. [38] proposed a nonlinear model prediction control model for electric driven car A/C system and implemented it as an interpreted MATLAB Simulink function block, which can be solved numerically using the *Model Predictive Control Toolbox*. The performance is validated with CoolSim high fidelity model, which is based on the Simulink model developed by Kiss et al. [39]. The prediction model is motivated by heat balance method [13].

### 2.2.4 Fuzzy Control

Fuzzy control is based on fuzzy logic, a mathematical system that analyzes analog input values on a continuous scale between 1 and 0 (true and false). This is in contrast to classical logic, which operates on discrete values of 0 and 1. As a result, fuzzy logic can deal with scenarios that cannot be simply expressed in binary terms, which are very common in the real world. The advantage of fuzzy logic is that human experience can be used in the design of the controller, making it easier to control tasks that have been performed by humans. Therefore, fuzzy logic control is suitable for A/C system AUTO mode, where thermal comfort is an important metric.

Research often focuses on the efficiency improvement over classical controllers such as PID and MPC controllers. Ku et al. [40] aimed to address increasing air conditioning efficiency by using predicted mean vote (PMV) as a thermal comfort index. The control logic is designed in conjunction with this metric. The researchers measured PMV performance

and energy consumption of the A/C system by implementing inverse PMV model with PID, self-tuning MPC controllers and fuzzy controllers, respectively. While all three methods obtained better results, fuzzy controller performed the best in terms of energy consumption. Furthermore, the detailed evaluation of PMV index is presented, along with mathematical derivations and block diagrams of three control methods.

Soyguder et al. [41] explored the possible way for fuzzy logic to integrate with traditional feedback controllers in A/C system. They designed a self-tuning PID-type fuzzy controller with gain values being adjustable by using fuzzy rules. The proposed controller has the same structure as a PID controller, so it can be easily integrated with the original control system while still having the benefits of on-line tuning. Additionally, they described how to build such an expert HVAC system and to perform numerical simulations in MATLAB/Simulink's *Fuzzy Logic Toolbox*. The performance, in terms of steady-state error and settling time, is better than PID controller and PD-type fuzzy controller.

The input parameters to fuzzy controller were studied by Farzaneh et al. [42]. In designing the vehicle cabin thermal model, the authors took blower power and mode door position into consideration to reflect the thermal comfort PMV index; the simplified PMV index only included cabin temperature and air velocity as its factors. Still, when comparing the two fuzzy controllers, one with temperature feedback and the other with PMV feedback, the latter showed better efficiency in terms of evaporator cooling capacity. The fuzzy controller was further optimized using genetic algorithm (GA); robustness analysis against ambient temperature variation was also performed.

Researchers developed fuzzy control logic based on the metrics of different thermal comfort models. Ibrahim et al. [43] employed the ANSI/ASHRAE Standard 55 by including temperature and relative humidity into the building of membership functions and fuzzy rules of the PD-type fuzzy controller. The strategy was employed to first bring the cabin temperature to a level within the comfort zone of relative humidity and then close the difference between the measured relative humidity and ideal value.

# Chapter 3

## Thermal Systems Modelling

Fully virtual product development requires thermal system models that are able to simulate the actual performance of the A/C system on a particular vehicle. It is crucial to identify the underlying physics, since thermal systems serve as the foundation for developing control logic and controllers. In this chapter, the step-by-step procedures for thermal systems modelling are laid out: from components building, system assembly to thermal systems integration and calibration.

The vehicle platform considered for this thesis is a SUV vehicle. There are two closed-looped thermal systems to be modelled: the A/C refrigerant loop and the vehicle cabin air loop. The two systems are individually built and calibrated using experimental data taken from the drive cycle test before they are joint together to form a complete thermal model.

The A/C refrigerant loop is a vapour-compression refrigeration cycle that consists of a compressor, a condenser, a TXV and an evaporator. To build each component, the physical geometry, capacity and performance data are acquired from the manufacturers. The software normally models the physical behaviours of well defined components with high accuracy; nonetheless, the components are calibrated against the performance data provided by manufacturers' data sheets. All major components are connected to form a closed-loop thermal system, which is further calibrated using data acquired from drive cycle tests performed on the actual vehicle in the environment chamber. Drive cycles are described in Section 3.2.

The vehicle cabin air loop represents the bulk of moist air inside vehicle cabin and it is subjected to properties and geometries of interior materials and glasses, thermal loads and vehicle operation conditions. Heat load enters the vehicle cabin through metal surface and glasses by radiation, external convection and conduction; thermal interactions between the interior materials and the air is mainly due to internal convection. The thermal mass is carefully calibrated during hot-soak and cool-down process which will be discussed in

#### Section 3.3.4.

When the two closed-loop thermal systems are connected together, they interact with each other on the evaporator level. That is, the refrigerant loop outputs evaporator outlet air condition to the cabin air model; cabin temperature is fed back as evaporator inlet air condition to the refrigerant loop. During the research, the refrigerant loop is approached first, followed by the cabin air loop. However, there is no requirement for the sequence of modelling the two thermal systems, as they can be built and calibrated independently using drive cycle data. The following are some considerations regarding modelling sequence:

- The refrigerant loop contains fewer components and involves simpler physics than the cabin air loop, hence its virtual model is easier to build.
- A high quality refrigerant loop virtual model can replace the drive cycle data in calibrating the cabin air loop.
- The controller strategy is applied on the refrigerant loop. A complete refrigerant loop model makes it possible to test the controller design at an early stage.

### **3.1 A/C Refrigerant Loop**

The A/C refrigerant loop is a 1D, closed-loop thermal system and it operates in vapour-compression refrigeration cycle. The purpose of the refrigerant loop is to remove unwanted heat and moisture from cabin air in order to maintain a certain comfort level for passengers.

The liquid refrigerant used for this study is R-1234yf. Being a more environmentally friendly alternative to R-134a in automotive A/C systems, it only has a global warming potential (GWP) index of less than 1; in contrast, this index for R-134a is 1430 [44]. The refrigerant exists in the loop as a two-phase flow and undergoes phase changes mainly in the heat exchangers. When modelling and calibrating the refrigerant loop, it is critical to ensure that the state of refrigerant flow does not exceed its physical limits. Thanks to the sensors placed throughout the loop, real time state of the refrigerant can be observed during simulation.

In addition to the four basic components (compressor, condenser, TXV and evaporator), The vehicle also has a built-in internal heat exchanger (IHX) to improve the thermal efficiency of the A/C system. IHXs are often found in stationary A/C system applications and recently are adopted in automotive applications as well. An IHX is a liquid-to-vapour heat exchanger (HEX) device that transfers heat from liquid refrigerant coming out from the condenser to vapour refrigerant coming out from the evaporator. The warm liquid gets

*sub-cooled* below the condensation temperature, while on the other side of the chamber, the cold vapour gets completely vaporized. As a result, the IHX helps improve the A/C system efficiency by saving compressor work.

The pressure-enthalpy (P-h) diagram for a simplified non-ideal vapour-compression refrigeration cycle is shown in Figure 3.1. The compressor work goes into the refrigerant flow during stage 1-2 by compressing the already superheated flow; from stage 2 to 4, the refrigerant transfers heat to the ambient air, undergoing a phase change while maintaining constant pressure; the expansion process happens right next, bringing down both pressure and temperature; finally, the refrigerant flow enters the evaporator as saturated mixture and completely evaporates by absorbing heat from the cabin air. The two phase changes in the HEXs along with the throttling effect of TXV and the work of compressor form the complete refrigeration cycle. It is important to make sure that the refrigerant flow entering the compressor must be completely superheated vapour, otherwise it may damage the compressor pump.

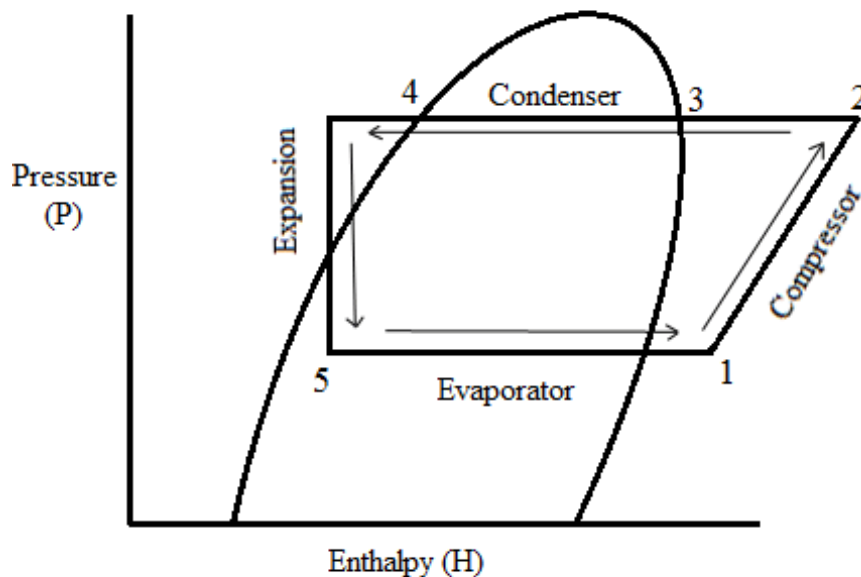


Figure 3.1: P-h diagram of a non-ideal vapour-compression refrigeration cycle [1]

The schematic view of the refrigerant loop is shown in Figure 3.2. Despite being simplified for better presentation, the major components along with input and output conditions can still be seen. There are three input conditions to the system: the compressor speed (rpm), condenser inlet air condition and evaporator inlet air condition; the only output is evaporator outlet air condition. Thermal sensors are placed before and after components,

allowing constant monitoring of refrigerant flow state.

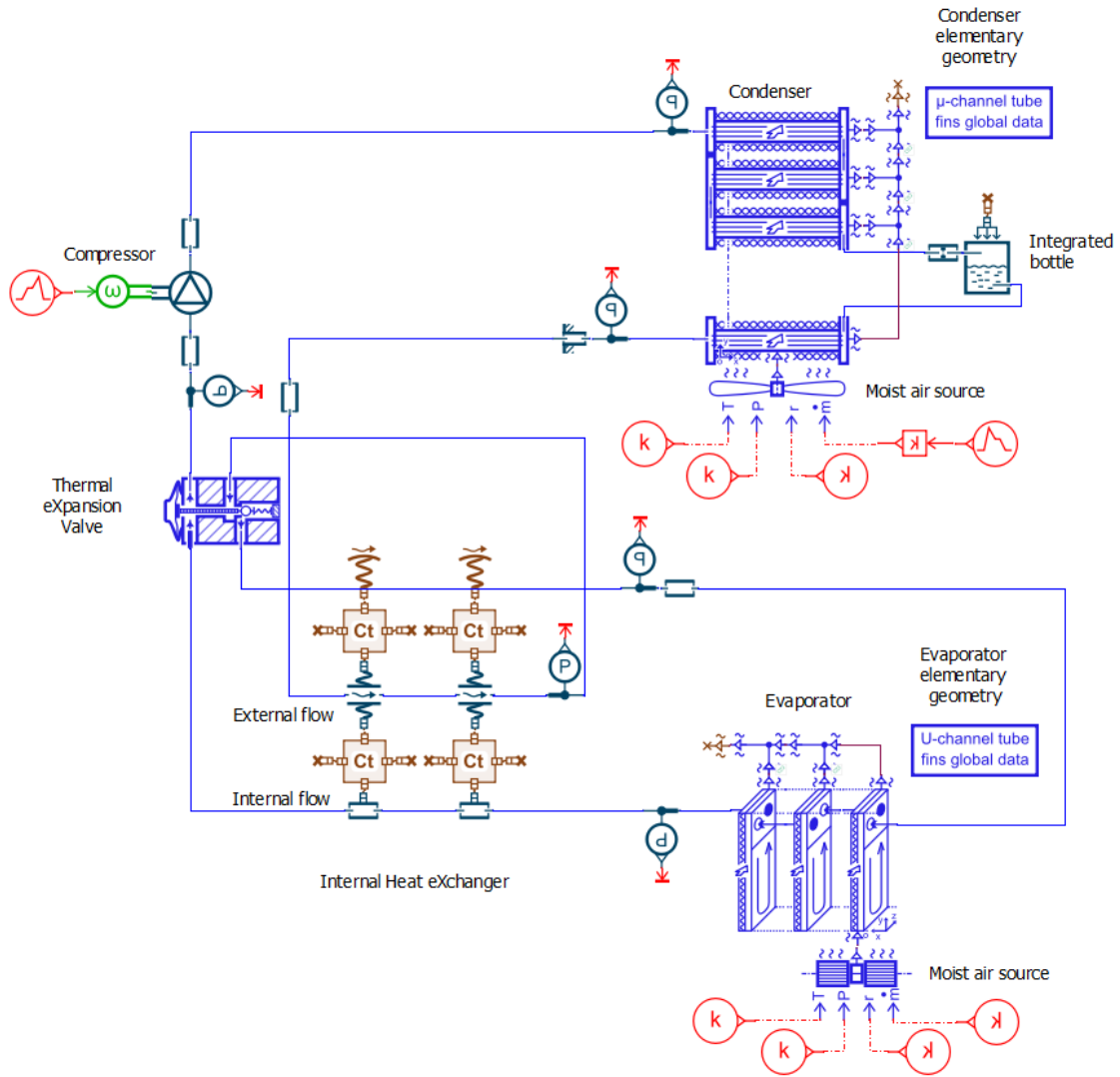


Figure 3.2: A/C refrigerant loop in Simcenter Amesim [2]

The refrigerant loop can operate under *fresh* mode or *re-circulation* mode. Under fresh mode, the evaporator inlet air comes directly from the ambient environment, hence it is possible for the refrigerant loop to work in the absence of cabin air conditions. However, re-circulation mode has better performance and conserves energy [45], therefore it is used during cool-down operation. The analysis will be based on re-circulation mode, as it is the case for drive cycle test. The dynamic cabin air condition is supplied by experimental data from drive test for model calibration.

### 3.1.1 Compressor

The compressor's role is to compress gaseous refrigerant and generate flow rate. Mechanical power from the engine crankshaft is converted to potential energies of the refrigerant in forms of pressure rise and temperature increase. As a side effect, the compressor also drives the refrigerant to circulate inside the loop, providing the flow rate. The refrigerant flow enters the compressor's suction port and comes out from its discharge port. The state of the flow remains as superheated vapour throughout the entire component. The compressor is driven directly by the running engine; the compressor's rotary speed is linked to the engine speed due to a fixed pulley ratio.

The compressor is a variable displacement piston compressor with a supplier-defined minimum displacement and a maximum displacement. The piston displacement is determined by the piston's stroke, which depends on the swash plate angle. The angle variation of the swash plate is regulated by an internal regulation valve, following the pressure conditions at suction and discharge ports. Ideally, the variable displacement feature helps the compressor to operate smoothly despite the engine's speed fluctuations.

Control strategies can be applied to the variable displacement compressor to regulate refrigerant flow temperature, eventually achieving a target evaporator air outlet temperature. In the basic form, a feedback controller reads the actual temperature of the air coming out of the evaporator and compares it with target temperature (reference signal). The controller issues a signal between 0 to 1, where 0 means the compressor is at the minimum stroke and 1 means the compressor is at maximum stroke. Therefore, the controller controls compressor's displacement to track the reference signal.

The physical geometries and efficiencies of the compressor are provided by the manufacturer for the working range of the pressure ratio and rotary speed. The volumetric efficiency  $\eta_{\text{vol}}$  and isentropic efficiency  $\eta_{\text{is}}$  are defined in 3D look-up tables provided later in this Section; these values depend on the pressure ratio  $\tau$  described in Equation 3.1 (pressure difference between the suction and discharge ports), rotary speed and fluid temperature. The mechanical efficiency of the compressor depends on engine rotary speed and pressure ratio in theory; it is set to a constant number according to the supplier's data sheet.

$$\tau = \frac{P_{\text{dis}}}{P_{\text{suc}}} \quad (3.1)$$

Equation 3.2 describes the volumetric efficiency  $\eta_{\text{vol}}$  for the compressor, where  $\dot{V}_{\text{real}}$  is the measured volume flow rate generated by the compressor at the discharge port. In reality, mass flow rate can be used in place of volume flow rate.

$$\eta_{\text{vol}} = \frac{\dot{V}_{\text{real}}}{\dot{V}_{\text{theory}}} = \frac{\dot{m}_{\text{real}}}{\dot{m}_{\text{theory}}} \quad (3.2)$$

The theoretical maximum volume flow rate  $\dot{Q}_{\text{theory}}$  is calculated in Equation 3.3, where  $\omega$  is the rotary speed and  $V$  is the displacement of the compressor. The displacement modulation factor  $\alpha$  of the variable displacement pump is determined by the control signal from feedback controller.

$$\dot{Q}_{\text{theory}} = \alpha \cdot \omega \cdot V \quad (3.3)$$

Equation 3.4 describes the isentropic efficiency  $\eta_{\text{is}}$ , which is defined as the ratio between the isentropic enthalpy variation and the real enthalpy variation between the discharge port and suction port.

$$\eta_{\text{is}} = \frac{\Delta H_{\text{theory}}}{\Delta H_{\text{real}}} = \frac{H_{\text{dis,isentropic}} - H_{\text{suc}}}{H_{\text{dis,real}} - H_{\text{suc}}} \quad (3.4)$$

As a result, the efficiency value can be determined at any combination of pressure ratio and compressor speed. The volumetric and isentropic efficiencies for the compressor in the working range speed and pressure ratio is presented by the 3D look-up table shown in Figure 3.3 and Figure 3.4, respectively. The horizontal axes represent the pressure ratio  $\tau$  and compressor speed in rpm, respectively. The vertical axis is the efficiency value. The values in between data sets are interpolated.

The basic structure of such a device can be found in the *Air-Conditioning* component library in Amesim software [2]. It should be noted that not all of the available parameters of the compressor are supported by Amesim, such as the suction and discharge ports geometries. This will not be much of a concern in terms of system performance accuracy, as the refrigerant loop as a whole will be calibrated once every component is modelled.

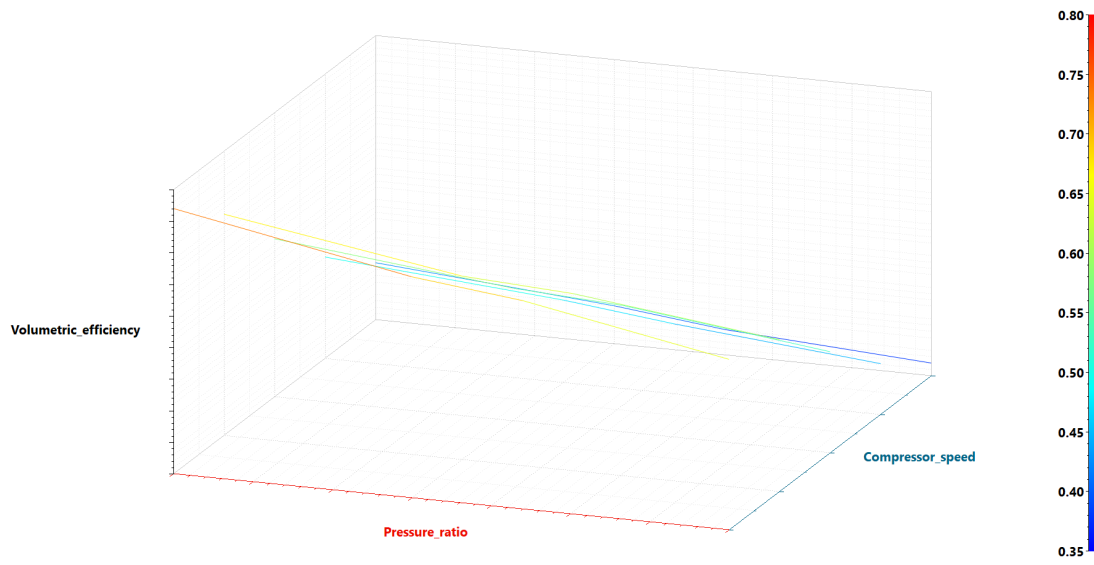


Figure 3.3: Compressor volumetric efficiency 3D look-up table.

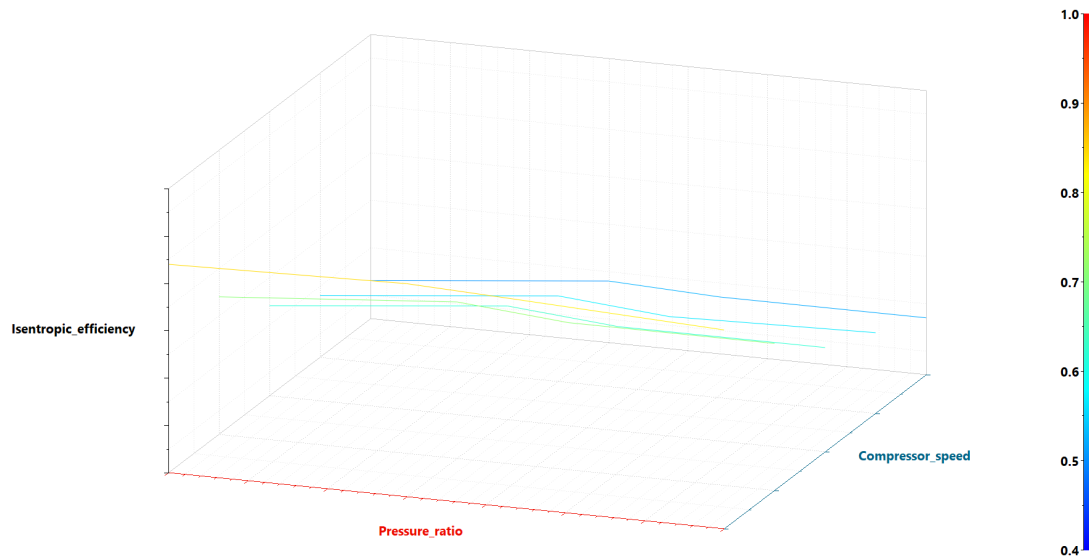


Figure 3.4: Compressor isentropic efficiency 3D look-up table.

### 3.1.2 Condenser

The three heat exchangers that exist in the refrigerant loop are the condenser, evaporator and internal heat exchanger. Both the condenser and evaporator involve complex heat transfer between refrigerant fluid and the air. Not only the geometries of the heat exchangers have to

be supplied, but suitable heat transfer correlations must also be selected in order to calibrate the virtual model against experimental performance data.

The condenser used in the vehicle is a fin-and-tube heat exchanger with a specified frontal area. The schematic diagram of such a condenser is shown in Figure 3.5. Each one of the four passes is represented by an identical sub-component found in the *Heat* library in Amesim. Geometric parameters shared among the passes include but not limited to fin length, fin pitch, hydraulic diameters, refrigerant-side tube cross-sectional area and air-side fin cross-sectional area. The most downstream pass shown at the bottom of the figure is subjected to vehicle speed input.

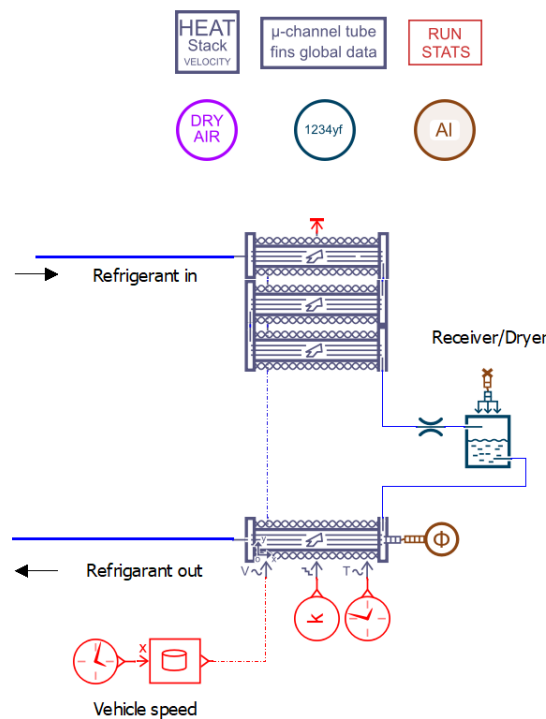


Figure 3.5: Condenser in Simcenter Amesim

Heat transfer in a heat exchanger typically involves heat convection in each fluid and heat conduction through the wall separating the two fluids. The heat transfer rate between the two fluids at a certain location in a heat exchanger depends on the magnitude of the temperature difference. Since the temperature difference often varies along the heat exchanger, accurate modelling of a heat exchanger can be challenging. Fortunately, air velocity and air-side condenser grid surface temperature can be found in experimental data taken at different vehicle speeds. The condenser inlet air condition depends on the vehicle speed, which is a changing value. Furthermore, when the air reaches the condenser, the temperature

and velocity are different from the ambient due to grille and under-the-hood effect. To compensate for that, experimentally determined 4D look-up table shown in Figure 3.6 is used for locating condenser grid surface temperature on a specific spot at a specific vehicle speed.

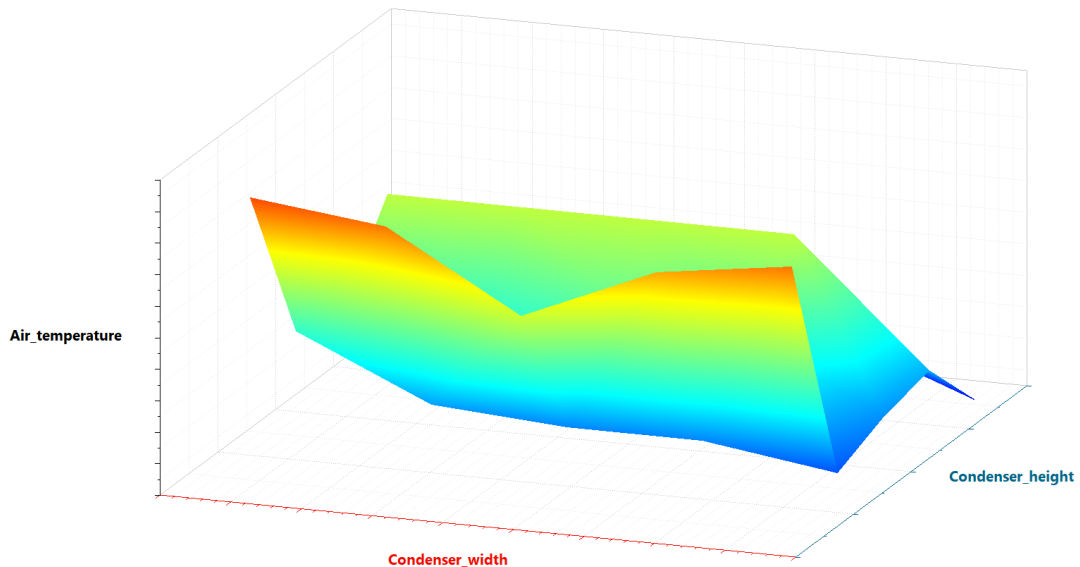


Figure 3.6: Condenser temperature 4D look-up table at a fixed vehicle speed

In the 4D table, condenser frontal surface dimensions in meters are represented in the two horizontal axes; the vertical axis is condenser grid surface temperature in degree Celsius. The fourth axis, vehicle speed in mph, is not possible to be shown in the figure and it forms the fourth dimension. The temperature distribution is recorded at three different vehicle speeds. In Figure 3.6, the results for only one speed is shown. Again, interpolation technique is used to find y value on any point of the condenser surface for any vehicle speed falling in the range of the three speeds. A very similar 4D table also exists for air velocity. The two tables are supplied to the condenser assembly to help determine local heat transfer rate for better modelling accuracy.

With physical geometries and air side conditions available, the next step is to calibrate the condenser so that the performance of the virtual model is as close to the physical unit as possible in its operating range. Heat rejection to the air causes the refrigerant flow to go through phase change; consequently, friction occurs and causes refrigerant-side pressure drop. Furthermore, pressure drop modifies the saturation pressure of the refrigerant, which has an impact on the heat rejection. As a result, heat rejection and pressure drop are coupled

and needed to be calibrated simultaneously using an iterative approach.

Heat rejection on the air-side is shown in Equation 3.5:

$$\dot{Q}_{\text{rejected}} = \frac{\text{Nu} \cdot k_{\text{air}}}{C_d} \cdot A \cdot (T_{\text{air}} - T_{\text{wall}}) \quad (3.5)$$

The convective heat transfer coefficient is defined by Nusselt number  $\text{Nu}$  in turbulent regime, with  $k_{\text{air}}$  being air-side thermal conductivity and  $C_d$  being air-side hydraulic diameter. The heat rejection is therefore associated with Nusselt number  $\text{Nu}$ . Other parameters include air-side surface area  $A$ , the temperatures of the air and the wall.

The Nusselt correlation in turbulent regime shown in Equation 3.6 is an expression comprised of Reynolds number  $\text{Re}$ , Prandtl number  $\text{Pr}$  and the coefficients  $a$ ,  $b$  and  $c$ :

$$\text{Nu} = a \cdot \text{Re}^b \cdot \text{Pr}^c \quad (3.6)$$

The three coefficients are used to tweak the external heat transfer to take into account different types of fin geometry. In case that the airflow is in laminar regime, a minimum Nusselt number is used in place of the correlation. The equations used to evaluate coefficients  $a$  and  $b$  are expressed in Equations 3.7 and 3.8.

$$a = \frac{\text{Nu}}{\text{Re}_1^b \cdot \text{Pr}_1^c} \quad (3.7)$$

$$b = \frac{\ln\left(\frac{\text{Nu}_1}{\text{Nu}_2} \left(\frac{\text{Pr}_2}{\text{Pr}_1}\right)^c\right)}{\ln\left(\frac{\text{Re}_1}{\text{Re}_2}\right)} \quad (3.8)$$

Note that at least two experimental points are needed to calibrate  $a$  and  $b$ . Calibration process involves adjusting  $a$  and  $b$  separately to obtain the desired value of condenser efficiency (measured by sub-cooling or power exchange rate). The value of  $c$  is kept default at 0.4, which is a good initial value according to a Amesim developer's suggestion [46] for setting up batch simulation to find the rest of coefficients.

By definition, Reynolds number  $\text{Re}$  is the ratio of inertial forces to viscous forces within a fluid which is subjected to relative internal movement due to different fluid velocities, as shown in Equation 3.9:

$$\text{Re} = \frac{\rho u L}{\mu} = \frac{\dot{m}_{\text{air}} \cdot C_d}{A_{\text{cs}} \cdot \mu} \quad (3.9)$$

Prandtl number  $\text{Pr}$  is the ratio of momentum diffusivity to thermal diffusivity and can be simplified into the form shown in Equation 3.10, where  $\mu$  is the dynamic viscosity and

$C_p$  is the specific heat of air.

$$\text{Pr} = \frac{\mu \cdot C_p}{k_{\text{air}}} \quad (3.10)$$

The refrigerant may undergo phase changes such as boiling and condensation. The refrigerant inside the condenser will most likely condense and therefore the overall heat transfer coefficient is calculated based on a full liquid heat transfer coefficient. Based on Amesim User's Guide [2], Shah correlation is used to calculate internal convective heat transfer coefficient in condensation situation. Nonetheless, correlation for boiling process should also be set up as the refrigerant may experience both condensation and boiling inside the tubes. VDI for vertical tubes correlation suites the application for single phase refrigerant flow in laminar regime. In this correlation Nusselt number  $Nu$  is kept constant at 3.66 for circular duct geometry. To verify the refrigerant flow regime, Reynolds number for flow in a pipe can be calculated using Equation 3.11, where  $u$  is the mean velocity of the fluid,  $C_d$  is the hydraulic diameter of the pipe and  $\nu$  is the kinematic viscosity. During normal operation the refrigerant flow is in laminar regime.

$$\text{Re} = \frac{u \cdot C_d}{\nu} \quad (3.11)$$

Although refrigerant-side heat exchange is calculated with pre-defined correlations, in some cases it may be necessary to adjust the internal heat exchange by modifying the refrigerant-side heat transfer gain “kHeat” parameter. Similarly, the friction occurring along the passes of the heat exchanger can also be manually adjusted with the refrigerant-side frictional pressure drop gain “kdP” parameter. The following step-by-step procedure for heat exchanger calibration was adopted in this thesis:

1. Build the heat exchanger using physical geometries and supply experimentally determined 4D look-up tables of air velocity and heat exchanger surface temperature at different vehicle speeds.
2. Choose Nusselt correlation for air-side heat rejection, set up initial values for Nusselt correlation coefficients, refrigerant-side pressure drop gain and refrigerant-side heat transfer gain.
3. Set up batch run to let the solver find a suitable combination of parameters to ensure minimum deviation from experimentally determined heat rejection and pressure drop values provided by heat exchanger manufacturer.
4. Iterate the previous two steps if necessary to reduce deviation.

The results for condenser calibration in Amesim is shown in Figure 3.7. The simulated results follow the trend of the supplier provided experimental data sets quite well. The heat rejection results show that the maximum deviation is merely 2.11% and the pressure drop deviation is 18.39%.

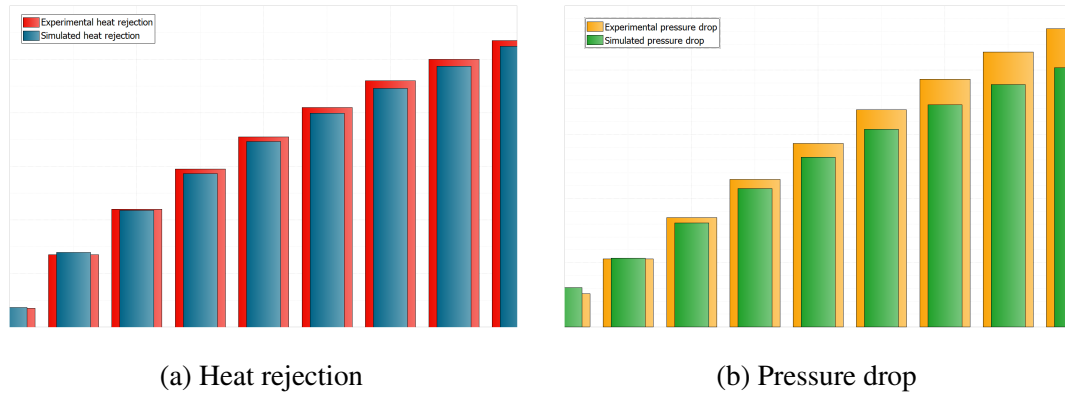


Figure 3.7: Condenser calibration

There is also a receiver dryer component located at the condenser outlet to remove any moisture from the refrigerant. The internal diameter and height, hence the volume information is available from the supplier. A stratified chamber component and an orifice from *Two-phase flow* library are used to model the receiver dryer. Note that the stratified chamber component in Amesim is ideal with no frictional losses, hence non ideal behaviours such as pressure drop are accounted for by the orifice. The ideal filtering process is adiabatic and constant-pressure, resulting in no heat exchange between the refrigerant and the ambient environment. The liquid and vapour phases inside the chamber have different densities in their respective volumes but they share a homogeneous pressure. More importantly, the receiver dryer is responsible for holding the excessive refrigerant flow when the cooling load is low. The height of the liquid inside the chamber is monitored.

### 3.1.3 Evaporator

The procedure for modelling and calibrating the evaporator is similar to the one used for the condenser, as both the evaporator and the condenser are liquid-gas heat exchangers involving refrigerant phase change. The evaporator on the vehicle is also a fin-and-tube type heat exchanger. The rows are arranged such that the front row has the same number of passes as the rear row to ensure optimal thermal performance. Unlike the condenser, there is no flow conditioning unit attached to the evaporator. Selecting the component from Amesim library becomes a simple task as to employ a dual-core heat exchanger. The same set of

geometric properties are supplied to the heat exchanger building tool but without the need of 4D look-up tables, since air-side conditions can be obtained directly from the cabin air model and blower fan.

The air-side conditions include air mass flow rate, temperature, pressure and density. The air mass flow rate is determined by the blower motor and fan assembly. For calibration purposes, the air mass flow rate is provided by the drive cycle experimental data. Air temperature can be considered the same as cabin air temperature, since the A/C system operates in re-circulation mode. Pressure is considered the same as the atmosphere; density is assumed to be constant as it does not vary significantly with temperature. Nusselt correlation shown in Equation 3.6 is used for evaporator air side heat rejection.

In contrast to the condenser, refrigerant flow inside evaporator tubes will be facing boiling condition. The overall heat transfer coefficient is calculated depending on the contribution of nucleate boiling as well as forced convection. VDI for horizontal tubes correlation is used when boiling occurs. Other correlations relationships used for refrigerant side heat transfer are the same as the ones used for condenser.

Similar to the calibration of condenser, refrigerant-side pressure drop gain “kdP” and heat transfer gain “kHeat” can be adjusted manually or automatically. The calibration process is to find a set of Nusselt coefficients, heat transfer gain and pressure drop gain to satisfy minimum deviation from supplier experimental data. The calibration working panel for the evaporator is shown in Figure 3.8.

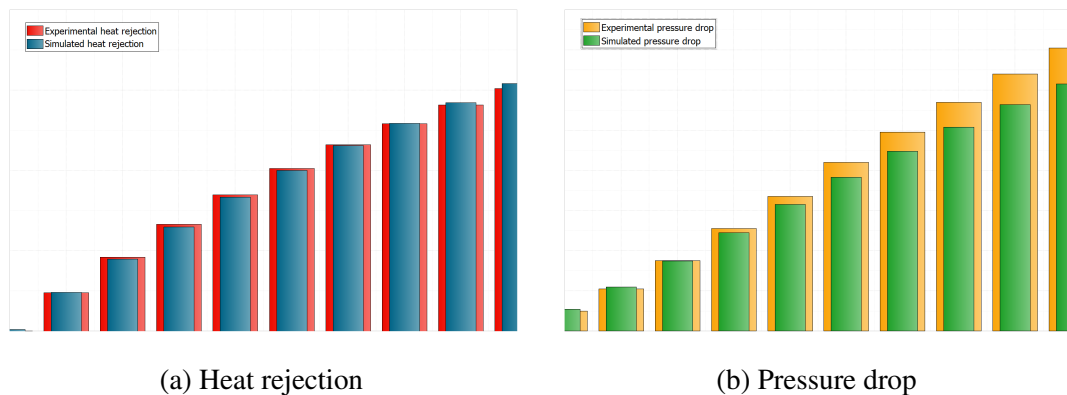


Figure 3.8: Evaporator calibration

It should be noted that heat rejection deviation has to be minimized as it affects the heat transfer rate between refrigerant and air, hence the actual performance of the heat exchanger model. Based on condenser and evaporator calibration results shown in Figure 3.7 and Figure 3.8, it can be seen that the heat rejection results are in good alignment with experimental data as deviations are at around 2%. Once the heat rejection is satisfied, pressure drop should

be kept within a reasonable range as it is only an internal behaviour of the refrigerant and does not have a direct impact on the performance. Pressure drop deviations are one order of magnitude larger at 18% and 12%, respectively.

### 3.1.4 Internal Heat Exchanger (IHX)

The internal heat exchanger works differently than condenser and evaporator where heat exchange happens between the refrigerant and the air. The two fluid branches inside an IHX are the warm refrigerant comes out of condenser and cold refrigerant comes out of evaporator. Heat exchange occurs between the warm and cold branches from the same closed loop, hence the name “internal”.

An important benefit of adding the IHX, besides improving thermal efficiency of the entire system by reducing compressor work, is that it acts as a double safe to ensure that the refrigerant is superheated before entering the compressor. The IHX will add additional heat to the refrigerant after the sensing bulb of the TXV. Normally the TXV is in charge of this and the refrigerant can be kept in the two-phase domain throughout the evaporator. The refrigerant temperature is thus homogeneous, resulting in an ease of designing the moist air flow piping, as well as a reduced computational complexity for evaporator virtual calibration. The requirement of refrigerant becoming completely superheated at compressor inlet, which used to be evaporator’s responsibility, is now ensured by the IHX.

Amesim software libraries do not contain a pre-defined “internal heat exchanger” component. Building the IHX becomes a manual task of adding thermal pipes to the two branches of the loop (to simulate flow friction and pressure drop) and sandwich an aluminum heat capacitor that conducts heat between thermal pipes of both branches. The detailed view of the IHX assembly is shown in Figure 3.9.

It should be noted that the heat transfer between pipes and the heat capacitor is by simple heat flux, hence complex convection correlation equations are not necessary. Since the geometries of the IHX is unknown, assumptions are made about the heat capacitor mass and the pipe geometries. The rate of temperature change shown in Equation 3.12 is based on energy balance of all four ports of the thermal capacitor, where  $\dot{q}_i$  is the input heat flux at the corresponding port in Watt.

$$\frac{dT}{dt} = \frac{\sum_{i=1}^4 \dot{q}_i}{m \cdot c_p} \quad (3.12)$$

The mass of the thermal capacitor does not have an impact on the performance for steady-state simulation. However, it will affect transient behaviour of the system. The

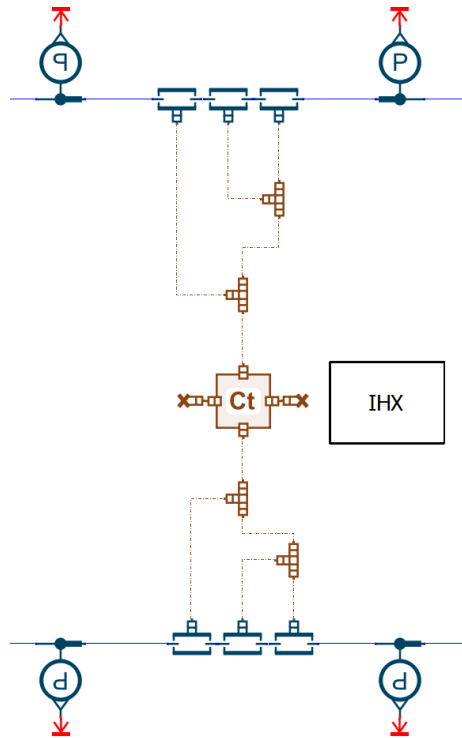


Figure 3.9: Internal heat exchanger detailed view

accurate modelling of the IHX relies on system calibration, i.e. charge initialization process. The state of the flow was monitored closely when performing system calibration to ensure that the refrigerant coming out of the evaporator is in two-phase state and that the IHX is in charge of superheating it.

### 3.1.5 Thermal Expansion Valve (TXV)

The thermal expansion valve (TXV) is an active metering device that regulates the refrigerant flow rate into the evaporator to ensure a near-constant superheat of the refrigerant vapour at the outlet of the evaporator. When the heat load on the evaporator increases, superheat at the evaporator outlet rises, and vice-versa. To avoid that, the TXV regulates the flow rate into the evaporator by altering its valve lift based on refrigerant pressures at the evaporator inlet, preloaded spring pressure and vapour pressure at evaporator outlet. Ideally, only the optimal amount of refrigerant is supplied by the valve to keep the entire evaporator surface active while not leaving any liquid refrigerant to be sucked into the compressor. The ability of the TXV to match the refrigerant flow to the rate at which it can be fully vapourized makes the TXV an ideal expansion device for air conditioning applications. The graphical representation of the TXV component is shown in Figure 3.10, with in-going, out-going

parameters and port numbers.

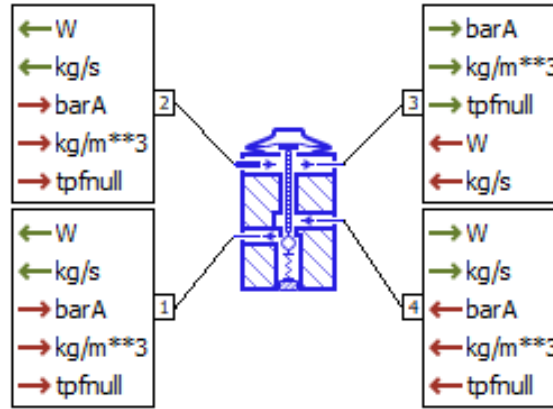


Figure 3.10: The thermal expansion valve component in Amesim

The TXV component from *Air-Conditioning* library has a total of four ports in two pairs, whose functions are described below. The refrigerant flow coming from the condenser enters port 4 and regulated flow exits port 1; at the evaporator outlet, flow enters port 2 and exits port 1. The port 2-to-3 pair on the top of the component is equipped with a thermal sensing bulb, which measures refrigerant pressure and converts it to its saturation temperature  $T_{bulb}$  by using a P-T chart. The pressure and density information received at port 2 is passed along to port 3 without any modification. The difference between actual refrigerant temperature and saturation temperature at measured evaporator outlet pressure is called superheat.

The valve regulates the flow between port 4 and port 1. A variable resistive element is implemented to simulate the force balance acting on the rod, described in Equation 3.13:

$$P_{evap,out}(T_{bulb}) = P_{TXV,in} + P_{spring} \quad (3.13)$$

The force balance on the valve lift involves valve opening forces (imposed by upstream refrigerant flow pressure and spring preload) and closing force (evaporator outlet pressure at bulb temperature). The resistive element can operate in the range from fully closed to fully open, depending on inlet pressure and the superheat measured at the sensing bulb between port 2 and 3.

The characteristics of the TXV are defined by the four-dimension diagram show in Figure 3.11. These quadrants are explained as follows:

1. The refrigerant saturation curve and valve opening curve as functions of evaporator outlet temperature and pressure is in quadrant 1. It defines valve opening pressure characteristics related to port 4 and port 2

2. The evaporator outlet pressure (port 2) as a function of valve lift (stroke in  $mm$ ) at  $0^\circ$  C bulb temperature ( $T_{bulb}$ )
3. The refrigerant mass flow rate (port 1) as a function of valve lift
4. The refrigerant mass flow rate as a function of evaporator outlet temperature

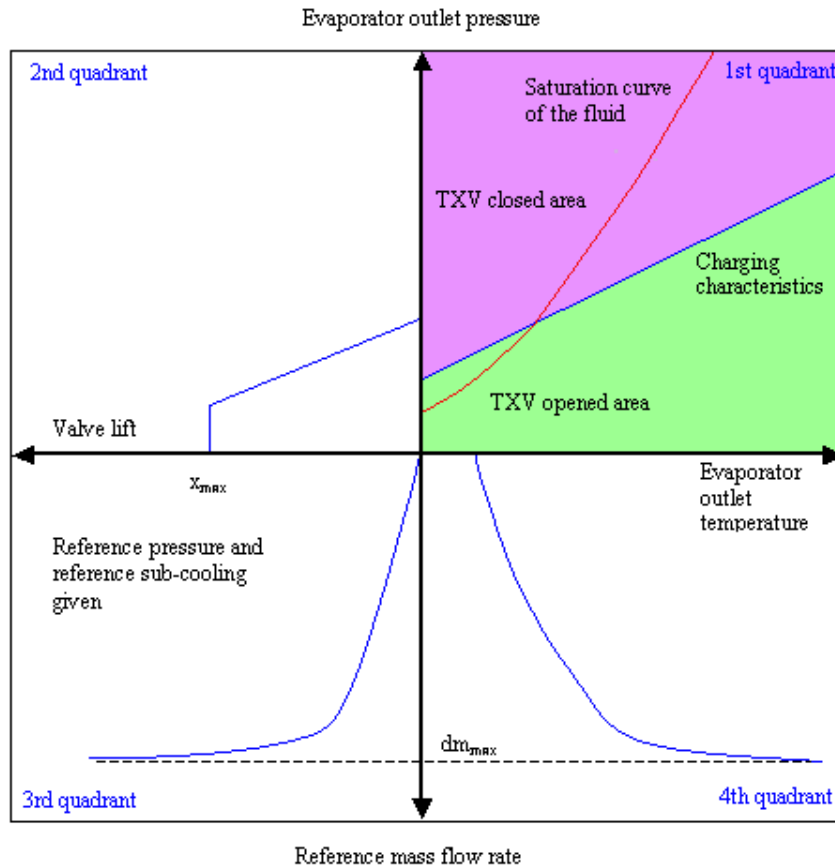


Figure 3.11: Four-dimension diagram for the thermal expansion valve [2]

The third quadrant shows the mass flow rate as a function of valve lift, provided high and low reference pressures at the TXV inlet and outlet ports, as well as reference sub-cooling. The fourth quadrant curve is derived based on the first and third quadrants, therefore 2D tables of the first three quadrants are needed from the supplier data. A pressure offset at bulb temperature is used to model the preload of the spring, hence in the first quadrant the valve opening curve can be shifted up or down. The maximum valve lift is explicitly specified by the supplier, limiting the maximum mass flow rate shown in quadrant 3 and 4. The mass flow rate imposed by the TXV is shown in Equation 3.14.

$$\dot{m} = \dot{m}_{\text{ref}} \cdot \frac{\rho}{\rho_{\text{ref}}} \cdot \sqrt{\frac{p_4 - p_1}{p_{\text{ref,high}} - p_{\text{ref,low}}}} \times \frac{\rho}{\rho_{\text{ref}}} \quad (3.14)$$

Where  $\rho$  is upstream fluid density and  $\rho_{\text{ref}}$  is the reference density computed based on the reference pressure and reference sub-cooling in third quadrant.

## 3.2 Drive Cycles

The basic approach to thermal systems modelling is to build A/C refrigerant loop and cabin air loop individually and calibrate them against the same set of experimental data until both systems are in good alignment with the physical performance. Charge initialization process on A/C refrigerant loop, for instance, requires external input as boundary conditions, such as ambient air conditions and vehicle speed profile. For cabin air model, more external parameters are going to be needed for thermal mass tuning. It is necessary to explain the experimental data taken from drive cycle test before jumping into the modelling of cabin air.

The experimental data comes from High Ambient AUTO mode drive cycle test performed on an actual vehicle. The drive cycle test is intended for capturing automatic A/C system performance under AUTO mode when the vehicle is subject to an extremely high ambient temperature and constant solar heat load. The target temperature for the cabin air is set to room temperature, and every other user modifiable option is set to AUTO. In particular, the ambient environment conditions specified by the drive cycle are listed as follows:

- Ambient temperature is extremely high.
- Initial cabin temperature is hot-soaked to a higher value.
- Relative humidity is low.
- Solar heat flux is constant and strong

During a cycle run, vehicle accelerates from still to city driving speed and maintains the speed for a while; it then accelerates to a higher speed and maintains the speed for the remaining of the test. The vehicle speed has a directly impact on A/C system performance: heat convection over condenser and other body parts. Also, it is worth mentioning that engine speed changes, which decides compressor speed.

The physical test is carried out in a thermal chamber with strictly controlled environment. The speed of the vehicle is ideally controlled by programmed robotic arm to avoid

extra thermal load imposed by the human driver. A turbine or fan is placed in front of the vehicle to simulate air flow at corresponding driving speed. During the test, various sensors and meters placed throughout the vehicle collect data relating various aspects of the operating condition of the vehicle.

### 3.3 Cabin Air Model

The vehicle cabin environment can be treated as a 1D model subject to solar radiation, ambient heat load and cold airflow from A/C refrigerant loop. Cabin air model is made up of cabin air volume, surface and interior materials, external and internal heat transfer dynamics during vehicle operation. The modelling of cabin air model follows a set of steps outlined as follows:

First, the air volume and thermal mass inside the cabin have to be quantified based on cabin geometries and interior dimensions. Physical and thermal properties of each material are also specified. Next step is to consider the heat load and assess the possible ways it can be transferred into the vehicle. Glass surface absorbs and transmits solar radiation depending on its absorptivity  $\alpha$ , reflectivity  $\rho$ , transmissivity  $\tau$  and incident angle; the transmitted radiation is absorbed entirely by interior materials. Opaque surfaces such as metal and plastic absorb solar radiation and at the same time are subjected to external forced convection, whose rate can be approximated based on vehicle speed and ambient air condition. Conduction also happens between engine compartment firewall and interior materials such as the dashboard. The last step is to calibrate internal convective heat transfer coefficients between air and interior materials. Hot-soak simulation pushes the system to an extremely hot initial condition, followed by cool-down simulation in which the transient behaviour of cabin air model can be observed and convective heat transfer coefficients can be tuned. The goal is to match the simulated cabin air temperature to drive cycle data. The processes described above can be carried out in an iterative manner to ensure a good tracking of cabin temperature.

An important remark is that according to High Ambient AUTO mode drive cycle, the A/C system is operated under re-circulation mode. The cabin air is circulated in a closed loop by the blower fan; the entire heat load is exhausted by heat exchange over the evaporator during vehicle operation.

### 3.3.1 Thermal Mass

The vehicle cabin interior is made up of objects and accessories such as seats, door panels and floor mats. They are of different shape, size and materials. Having larger specific heat than air, they act as a damper during transient behaviour, hence are called thermal mass. Both the transient and steady state behaviours of cabin model depend on its thermal mass composition.

- The volume of each interior object is estimated based on cabin CAD report from industrial partner, where the dimensions of each object are provided. The thermal mass can be easily determined knowing the density.
- Major objects inside the cabin include roof, firewall/dashboard, side panels, doors, rear panel, seats and carpet. Glass parts include windshield, rear shield and six door windows in three rows.
- The interior air volume is calculated by subtracting the volume of bulky interior objects such as seats and dashboard from the total cabin volume.
- Specific heat  $C_p$  and thermal conductivity  $k$  is assigned to each different material.
- For objects that are subjected to solar heat flux, the angles of the objects with respect to horizontal ground are measured. With the knowledge of solar flux angle with respect to the ground, incident angles can be determined.
- An additional mass is added to the virtual system to represent miscellaneous components with obscure dimensions, such as steering wheel and centre console. Moreover, the added mass acts as a tuner during the first few iterations of cool-down simulation, as often times the cool-down curve is too rapid due to the lack of thermal inertia in the virtual model. The role of this miscellaneous mass can be taken over once internal convective heat transfer coefficients are established and the masses of other components are adjusted.

### 3.3.2 External Heat Transfer

Heat load enters the cabin through thermal radiation and forced convection. The thermal radiation heat flux and ambient air conditions include temperature, pressure and relative humidity are described previously in Section 3.2.

The energy exchange mechanism of thermal radiation is characterized by Equation 3.15:

$$\alpha + \rho + \tau = 1 \quad (3.15)$$

Here, absorptivity is denoted by  $\alpha$ , reflectivity by  $\rho$  and transmissivity by  $\tau$ . Given incidental angle and the medium, these coefficients are a function of wavelength. For glass materials, the baseline values for the three properties at a perpendicular incident angle are provided by industrial partner. Note that the PVB plastic layer in the construction of windshield glass does not affect its thermal radiation properties; it only has an influence on density, specific heat and thermal conductivity. The reflectivity  $\rho$  determines the portion of radiation reflected by the material; since the values are very small compared to the other two, it is omitted in the modelling process.

Another thermal property of interest is emissivity  $\epsilon$ , which is defined as the ratio of the thermal radiation from a surface to the radiation from an ideal black body at the same temperature. Larger (closer to 1) value of emissivity indicates that the material cools itself better by emitting more thermal radiation. Emitting radiation is another way to cool down, in addition to heat convection by the air. The emissivity of the vehicle outer surface as a whole is assumed and it is to be defined separately in glass and metal surface properties.

Solar radiation not only interacts with vehicle surface materials, but also gets transmitted into the vehicle cabin through glasses. It is assumed that solar radiation through the windshield is absorbed entirely by the instrument panel; radiation through other windows and rear shield are absorbed by the seats and the headliner. This is based on the fact that the radiation emitted by the interior materials is trapped inside the cabin due to the blocking effect of windshields and glasses, known as greenhouse effect. For this reason, the cabin air temperature can rise to a much higher value than the ambient air temperature. It also explains the higher-than-ambient initial cabin air temperature at the beginning of the drive cycle.

The forced convection that happens on the surface of vehicle is modelled using “flat plate with predefined correlation” in Amesim. The input to this sub-model include ambient air conditions and vehicle speed. Schematic view of the vehicle cabin model constructed in Amesim is shown in Figure 3.12, showing the arrangement of thermal mass and corresponding heat transfer mechanisms. The details of internal convective heat transfer is described in section 3.3.3.

### **3.3.3 Internal Heat Transfer**

Inside the vehicle cabin, heat transfer happens mainly in the form of convection. The special case of radiation transmitted through glasses is previously discussed in Section 3.3.2.

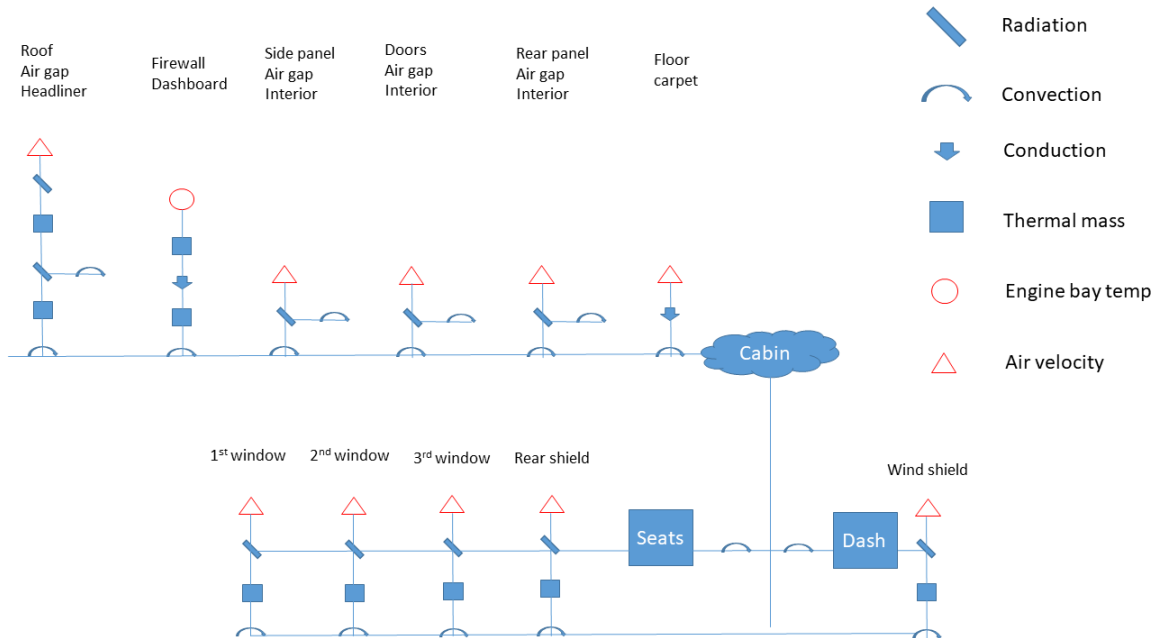


Figure 3.12: Schematic view of vehicle cabin model in Amesim

Internal convective heat transfer can be complex to model due to the fact that it not only involves heat load on different materials in a vertical space, but is also subjected to air distribution inside the cabin. To better model the local convective heat transfer, a slew of heat transfer coefficients are defined between materials and air.

The simplest case for internal convective heat transfer happens between the inner side of glasses and cabin air. Since the windshield, windows and the rear shield are made up of the same material and are on the same vertical height, the same convective heat transfer coefficient is assigned to all of them. This value is later to be determined in hot-soak and cool-down simulations.

Another group of interior objects sharing the same convective heat transfer coefficient include: firewall/dashboard, side panels, doors and rear penal. These inner surfaces are all made up of interior mat. The headliner attached to the roof is a special case as it is made up of canvas and that it is positioned at the top of the cabin volume; a separate coefficient  $h_{\text{headliner}}$  is assigned to it. Following the same logic, convective heat transfer coefficients for seats, carpet and miscellaneous thermal mass are defined, respectively.

During AUTO mode operation, the airflow provided by the blower is split up in the duct and sent through different air outlets. The instrument panel outlets get approximately most of airflow and floor outlets get the rest. Consequently, the instrument panel and floor are assigned with different convective heat transfer coefficients, as the difference in thermal mass and vertical distance of the two parts cannot be ignored. To be perfectly clear, the two

coefficients are applied in which convection happens between thermal masses and cold air coming out of the duct outlets; not to be confused with the cabin air volume in which other thermal masses interact with.

Air gaps are small air compartments that exist between the interior panels and outer surfaces, such as the vacant space found inside the door panel. The construction of such a mechanism is shown in Figure 3.13. To recap, solar radiation and external convection apply to the outer surface of the vehicle; the air gap between metal surface and interior mat is modelled using natural convective heat transfer correlation. On the inside, internal convection between door panel and cabin air is defined by a convective heat transfer coefficient.

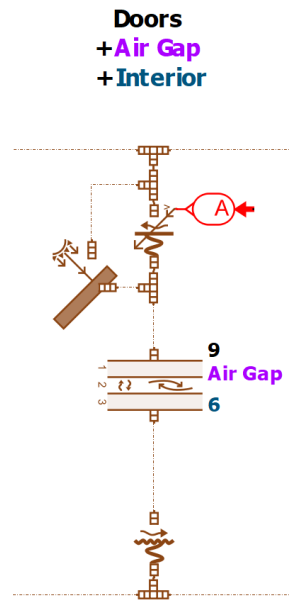


Figure 3.13: Air gap inside the door

Natural convection correlation is used for air gap convection analysis. The heat exchange rate from layer 1 to layer 3 (with air gap being layer 2) is defined in Equation 3.16:

$$\dot{Q}_{1-3} = h_{1-3} \cdot A \cdot (T_1 - T_3) \quad (3.16)$$

The heat exchange coefficient is computed with the Nusselt number as shown in Equation 3.17:

$$h_{1-3} = \frac{Nu \cdot k}{th} \quad (3.17)$$

where  $Nu$  is the Nusselt number in air layer,  $k$  is the thermal conductivity of the air in layer and  $th$  is the thickness of air layer.

### 3.3.4 Hot-soak and Cool-down

Internal convective heat transfer coefficients established in the previous two sections provide the means to calibrate cabin air model performance. When the coefficients are first established, their values are unknown due to the lack of knowledge on internal air velocity. To overcome the inherent shortcoming of 1D modelling, hot-soak and cool-down simulations are employed to find appropriate coefficients so that the virtual model could behave as close to High Ambient AUTO mode drive cycle as possible. Key steps for calibration process are listed below:

- Initial values of heat transfer coefficients are assumed and applied to the model. Set up the cabin model to simulate that the vehicle is parked in the hot ambient environment with engine turned off (disconnected from A/C refrigerant loop). Stop the simulation once cabin air temperature reaches set point, as specified by the drive cycle.
- Use the hot-soaked system prepared in the last step as initial conditions for cool-down simulation (connected with A/C refrigerant loop). Run the cool-down using drive cycle profile from the beginning.
- Compare transient behaviour of cabin air temperature in cool-down simulation against drive cycle experimental data; adjust heat transfer coefficients using built-in optimization tool in Amesim.
- The process can be carried out in an iterative manner to refine the coefficients for better performance of cabin air model: simply stop the cool-down simulation to apply the adjusted coefficients should cabin temperature deviates from experimental data; repeat hot-soaking again to get the new initial conditions for the next round of cool-down.

The optimization tool in Amesim relies on batch calculations to find the best combination of heat transfer coefficients. It is possible to define the range of each coefficient, specify desired accuracy and lock certain coefficients from being optimized. The algorithm of choice is NLPQL (Non-linear Programming Quadratic Line search), which is an iterative process based on the use of gradients. It tries to decrease the objective function to zero by computing the gradients of the objective function and constraints in all directions available in the design space (each input parameter involved in the optimization process is a direction) [2]. The outcome of the iterative optimization process is a set of heat transfer coefficients that is able to simulate cool-down temperature curve. The results are summarized in Chapter 5.

# Chapter 4

## Control Design

### 4.1 Methodology

The thermal systems modelled in Chapter 3 are capable of simulating the cabin air temperature during High Ambient AUTO mode drive cycle. The combined refrigerant loop and cabin air loop are supplied with drive profile, ambient environment conditions and blower fan air flow rate in standard cubic feet per minute (SCFM) recorded in physical drive test. The details of drive cycle are described in Section 3.2. The test is performed under an extreme high ambient temperature and high solar heat load; it starts when the cabin air is hot-soaked to a higher-than-ambient initial temperature. The target temperature is set to room temperature. During the test, the on-board A/C control unit determines the blower motor speed, hence the air flow rate over the evaporator.

In this chapter, efforts are made to construct a controlled DC motor assembly to supply optimized air flow rate to the thermal models. A PID controller is used to track the reference speed and issue voltage signal to the DC motor assembly using PWM technique. Linear system analysis is performed on the DC motor before it is implemented in MATLAB/Simulink. The PID controller is tuned in discrete time domain.

As a result, the controlled blower motor assembly tracks desired speed and generates air flow rate for the thermal systems, making the virtual model independent of experimental data. Additionally, the possibility of co-simulation between DC motor assembly in Simulink and thermal systems in Amesim is explored. Under co-simulation mode, the virtual model is able to run independently for any drive cycle, making it possible to simulate arbitrary drive cycles without the need for experimental data. However, constraints do exist such as the way thermal models are calibrated. The details will be discussed in Chapter 6.

## 4.2 DC Motor Assembly

A DC motor is an electrical rotary device that converts direct-current electrical energy into mechanical rotational energy by utilizing current-magnetism relationships. In its basic form, a DC motor consists of a magnetic source and an armature in which electric current runs through. The DC motor assembly consists of a brushless DC motor, a position/speed sensor, and three-phase converter. An axial fan is attached to the motor shaft to generate air flow and a discrete PID controller issues PWM signals to drive the DC motor assembly. The reference rotary speed is converted from experimentally recorded air flow rate in SCFM. Since the information on blower assembly is not available through the supplier, the design process takes knowledge and parameters from the literature such that the components are sized to fit automotive applications [47]. There are also known design constraints, such as the DC voltage supply is fixed at 14V (from car battery).

### 4.2.1 Linear System Analysis

The linear second-order equation of a DC motor is shown in Equation set 4.1, where the armature circuit is described by Equation 4.1a and the mechanical rotor by Equation 4.1b:

$$L_a \dot{I}_a + R_a I_a = e_{in}(t) - K_b \omega \quad (4.1a)$$

$$J \dot{\omega} + b \omega = K_m I_a - T_L \quad (4.1b)$$

The input variables are armature voltage  $e_{in}(t)$  and load torque  $T_L$ ; the output variable of interest is rotor angular speed  $\omega$ . It should be noted that the right-hand side of Equation 4.1a contains the induced back electromagnetic force (EMF) term  $K_b \omega$  that reduces the net voltage of the armature. Similarly, the net torque is reduced by external load torque  $T_L$ . The armature coil inductance  $L_a$  (due to the windings) and armature resistance  $R_a$  determine the size of the circuit; the rotor's moment of inertia  $J$  and friction coefficient  $b$  determines the size of the rotor. Note that the units for motor-torque constant  $K_m$  (N·m/A) and back EMF constant  $K_b$  (V·s/rad) are equivalent when expressed using the basic SI units. The two linear first-order equations are coupled and solved together, resulting in a second-order model. Supply with the voltage  $e_{in}$  and load torque  $T_L$  as input variables, the solution to the second-order model gives information on the angular speed  $\omega$ .

Low-order linear system is a well studied branch in the field control theory, in which analytical techniques built for dynamic system analysis can be applied to obtain the system response [47]. The system's analytical solution and transfer function provide information

on how various system parameters affects the system's response. Additionally, complex non-linear systems usually have dominant modes that can be approximated by linearized second-order system. As a result, analytical approach provides insight into building control strategy for the system. In MATLAB/Simulink, numerical approach is going to be applied despite the complexity of the system [48]. Still, understanding the model is vital in making right decisions in the design process. The parameters of DC motor and their values are summarized in Table 4.1.

Table 4.1: DC motor parameters

Parameter	Symbol	Value
Voltage	$e_{in}(t)$	14 V
Inductance	$L_a$	1.5 mH
Resistance	$R$	0.5 $\Omega$
Back EMF constant	$K_b$	0.04 V·s/rad
Motor torque constant	$K_m$	0.04 N·m/A
Motor moment of inertia	$J$	$2.5(10^{-4})$ kg·m <sup>2</sup>
Motor friction coefficient	$b$	$10^{-4}$ N·m·s/rad

The dynamic response of a second-order linear system can be studied by analyzing its transfer function in Laplace domain. The closed-loop block diagram shown in Figure 4.1 is a logical representation of DC motor's transfer function, with input voltage and output angular velocity. Note that it is not a feedback control system, as the fed-back term is merely the induced back EMF voltage (referring to the right hand side of Equation 4.1a).

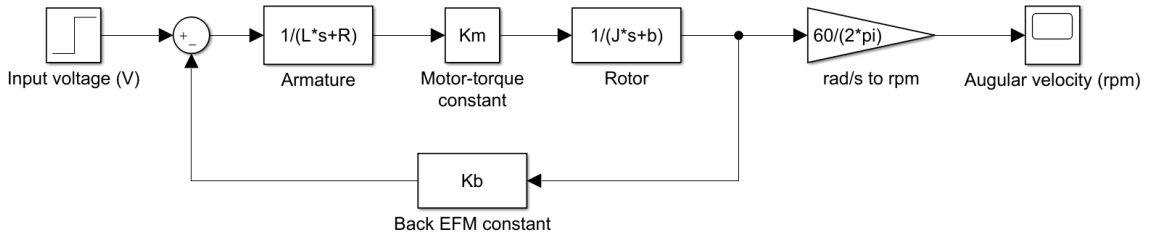


Figure 4.1: Block diagram of a DC motor' transfer function

By applying block reduction, the transfer function of DC motor is obtained as shown in Equation 4.2:

$$\begin{aligned}
G(s) &= \frac{K_m}{(Ls + R)(Js + b) + K_m K_b} \\
&= \frac{K_m}{LJs^2 + (Lb + RJ)s + (Rb + K_m K_b)}
\end{aligned} \tag{4.2}$$

The steady-state motor speed can be computed based on transfer function's DC gain, which is the value of  $G(s)$  with  $s = 0$ . The motor speed is a product of DC gain and input voltage. The 14V input results in a steady-state motor speed at 3240 rpm, which is adequate to satisfy the requirement of air flow rate (blower fan model is described in Section 4.2.7). The Laplace transform of the unit step input is  $E_{in}(s) = 1/s$ , hence the 14V voltage is  $E_{in}(s) = 14/s \Omega(s)$  as shown in Equation 4.3:

$$\Omega(s) = E_{in}(s)G(s) = \frac{14}{s}G(s) \tag{4.3}$$

Alternatively, final-value theorem can be applied to verify the steady-state output in order to find steady-state motor speed if voltage is used as system input, as shown in Equation 4.4:

$$\lim_{t \rightarrow \infty} \omega(t) = \lim_{s \rightarrow 0} s\Omega(s) = \lim_{s \rightarrow 0} sE_{in}(s)G(s) = \frac{14K_m}{Rb + K_m K_b} \tag{4.4}$$

The two poles of the transfer function are -319.9826 and -13.7507. respectively. The two negative real numbers indicate that the system's steady-state response is stable as time approaches infinity; the transient response is over-damped and does not show any oscillations due to the fact that there are no imaginary parts. Note that the system is initially at rest with initial conditions  $\dot{\omega}(0) = \omega(0) = 0$ . The system's response to a step input is the sum of two exponential functions shown in Equation set 4.5:

$$f_1(t) = e^{-319.9826t} \tag{4.5a}$$

$$f_2(t) = e^{-13.7507t} \tag{4.5b}$$

The time constants are calculated as  $\tau_1 = 0.0031 \text{ s}$  and  $\tau_2 = 0.0727 \text{ s}$ . Note that the settling time for any exponential function is equal to four times of its time constant, and that the system response follows the exponential function with the slowest settling time. Therefore, steady-state value is reached at  $t_s = 4\tau_2 = 0.2909 \text{ s}$ . The step response is plotted in Figure 4.2.

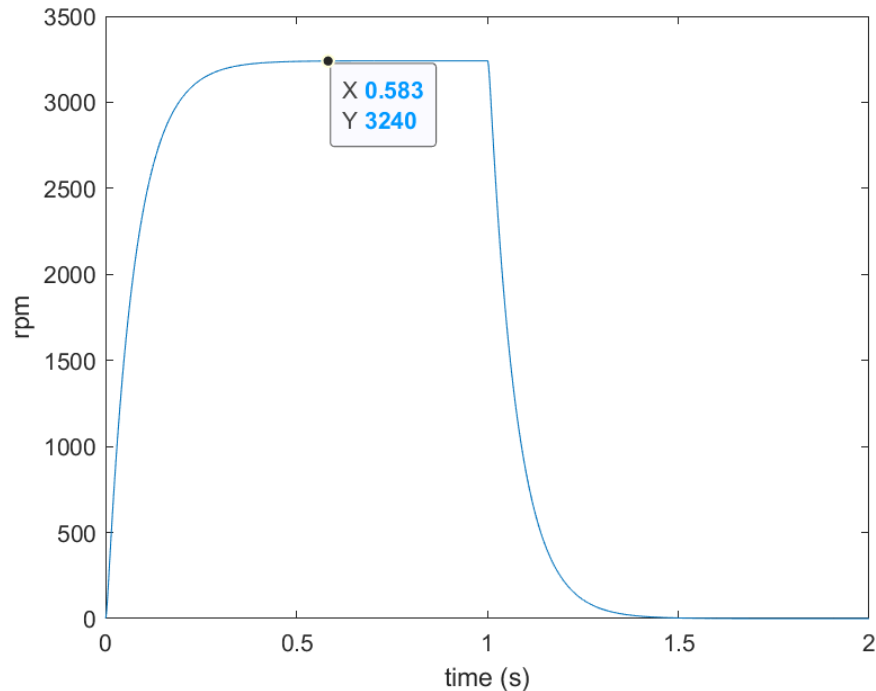


Figure 4.2: Step response of a DC motor

Deriving analytical equations can help understand the characteristics of the system and it is the first step towards control design. However, linear transfer function analysis may not be sufficient to exactly represent the real dynamics of the physical DC motor system due to modelling uncertainties such as mechanical friction. Besides, it is not always practical to rely on purely analytical approach, especially in a situation where discrete time domain and PWM technique are present. The following analysis of DC motor is based on models from Simulink's Simscape library, taking numerical approach to solve time-domain differential equations for system response.

### 4.2.2 Brushless DC Motor

On a conventional brushed type DC motor, the permanent magnet is stationary, called a stator; the armature that is wrapped in coil windings rotates around a shaft, hence it is called a rotor. The armature magnetic poles interact with the poles of the permanent magnet to make the rotor spin. At each half turn of the rotor, the rotor poles need to be flipped by mechanically switching the polarity of the current in the coil windings to keep the motor spinning. This is done by metal brushes attached to the shaft maintaining electrical contact between the voltage source and the rotating armature. The switching of current polarity is called commutation. Brushed DC motor has several drawbacks that make it unsuitable for

automotive applications. In particular, the commutation brushes wear out during operation, reducing motor’s lifespan. The efficiencies also suffer due to mechanical friction. Brushless DC motor, on the other hand, addresses these issues and are widely adopted by automotive HVAC applications.

On a BLDC motor, the armature is fixed while the permanent magnet (or electromagnet) is rotating around the armature. Consequently, the terminologies for brushless DC motor are the opposite of the ones for brushed motor, with armature being the stator and permanent magnet or electromagnet being the rotor. A three-phase inverter effectively replaces the role of metal brushes, conducting electronic commutation instead of mechanical commutation. The main advantages of BLDC motor include: low maintenance, quiet operation and higher efficiency. HVAC systems, especially those featuring variable-speed operation, use BLDC motor since the built-in control algorithm allows fine control over motor speed, hence air flow rate. The downside is the increased level of complexity: it requires sensor to monitor rotor’s rotating position and commutation logic to operate the three-phase converter so that the controller can precisely optimize motor speed. In real applications, PWM technique is often used for modulating a fixed voltage supply to alter motor speed [49]. PWM generating techniques and the concept of duty cycle are discussed in Section 4.2.6.

The block diagram for blower assembly is presented in Figure 4.3. The input to the system is desired fan speed in rpm, which is converted from required air flow rate based on blower fan’s SCFM-rpm curve. The output fan speed is again converted to air flow rate in SCFM. The control algorithm for the BLDC motor is an orchestration of motor controller, three-phase inverter, Hall sensor and commutation logic.

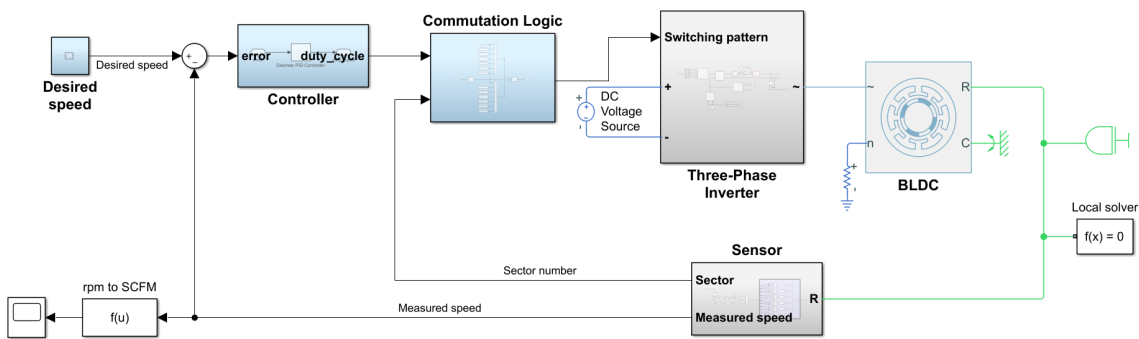


Figure 4.3: DC motor subsystem in Simulink

The specifications and geometries of the blower assembly on the vehicle are not made available by the supplier. Therefore, assumptions have to be made regarding the type of DC motor (brushless) and driving mode (PWM driven) in order to proceed with control design.

The BLDC motor that is going to be implemented in Simulink inherits the parameters of the example DC motor used for linear system analysis in Section 4.2.1. Additional parameters specifically for brushless type DC motor is list in Table 4.2.

Table 4.2: BLDC motor parameters

Parameter	Value
Number of pole pairs	4
Winding type	Wye-wound
Back EMF waveform	Trapezoidal
Permanent magnet flux linkage	0.1 Wb
Back EMF flat area	120/4 °
Sample time	$1 \times 10^{-5} s$
PWM switching frequency	10 kHz

### 4.2.3 Three-Phase Inverter

A three-phase inverter is a power electronic circuit that transforms direct current (DC) from the voltage source to alternating current (AC) and applies it to BLDC motor’s armature coils. The working principle of a three-phase inverter is as follows: consider a BLDC motor that has a permanent magnet rotor with one pair of north and south poles; the stator consists of three coils spaced at 120° apart from each other. At any time, two of the three coils are polarized by applying positive and negative currents across them so that magnetic field is artificially generated. The rotor is forced to align itself with the stator’s magnetic field. As the rotor’s position gets close to alignment, the phase (sign) of electric current applied to the coils is switched by three-phase converter, resulting in a revamped magnetic field. Hence, the electric commutation occurs in such a way that the rotor is forced to rotate constantly to re-align itself with stator’s magnetic field.

The name “three-phase” indicates that the inverter can energize two of the three phase coils with positive and negative current, respectively, and leaving the third coil not energized at all (no current applied). Therefore, for BLDC motor with one pole pair and three coils, there are six patterns to polarize any two of the three coils, and the commutation occurs every 60° of rotation. With more pole pairs and coils, commutation occurs more frequently. Commutation logic is explained in Section 4.2.5. The block diagram of a three-phase inverter is shown in Figure 4.4.

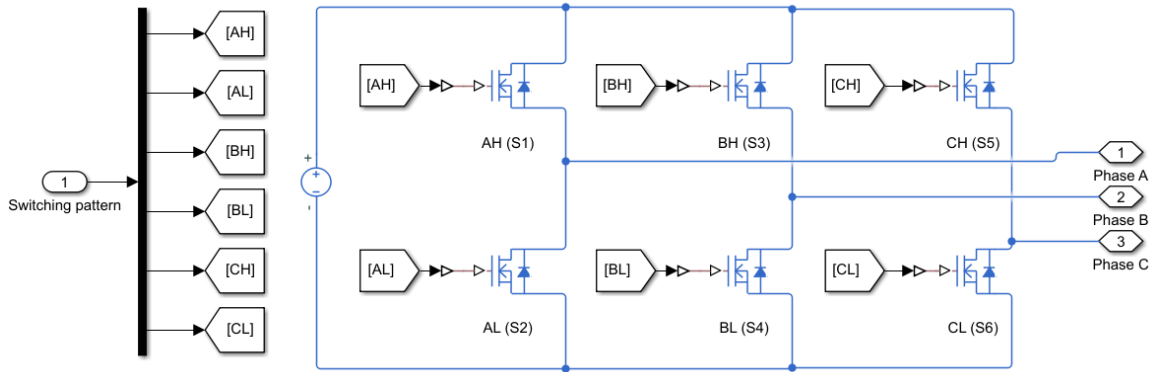


Figure 4.4: Block diagram for three-phase inverter

The three-phase inverter consists of six MOSFET (metal–oxide–semiconductor field-effect transistor) switches in three pairs, corresponding to three coils. Each switch pair has a high and low side to supply positive or negative current to the coil. At any rotor position, the input signal from commutation table turns each switch on or off so that one pair of coils are polarized to create a magnetic field, as shown in Figure 4.5.

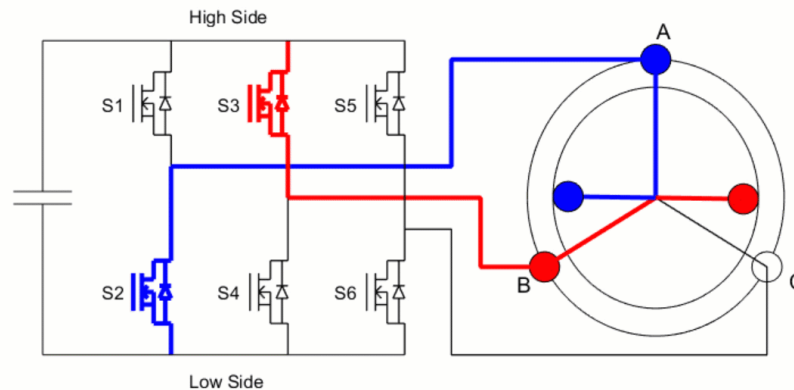
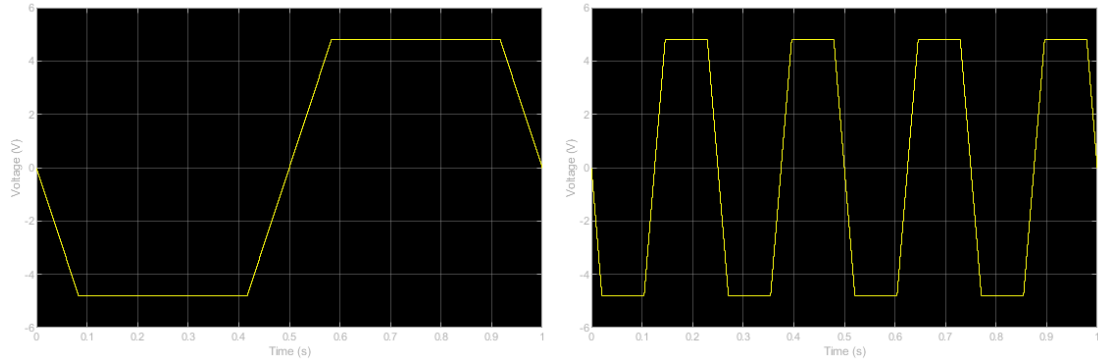


Figure 4.5: A pair of coils is polarized by three-phase inverter [3]

The BLDC motor used in this thesis contains 4 pole pairs and correspondingly 12 coils. Therefore, commutation occurs every  $15^\circ$  of rotation as opposed to every  $60^\circ$  in motor with single pole pair. In addition, motor's speed and torque fluctuations can be improved thanks to more frequent commutation. Figure 4.6 shows the comparison between back EMF profiles of BLDC motors with only 1 pole pair and 4 pole pairs.

During one revolution of the rotor, the induced back EFM on any one of the coils exhibits a trapezoidal shape, which repeats itself  $n$  times for BLDC motor with  $n$  number of pole pairs. Therefore, a smoother operation can be achieved with more pole pairs.



(a) Back EMF profile with 1 pole pair

(b) Back EMF profile with 4 pole pairs

Figure 4.6: Back EMF profiles with different pole pairs

#### 4.2.4 Hall Effect Sensor

To commutate the stator coils with correct phases at the right time, rotor position information is needed to determine the output signal of the commutation logic. Hall effect sensors are used to send voltage signals to indicate on and off states by sensing the magnitude of a magnetic field. The relative position of the rotor within one revolution is made available through the knowledge of the magnitude of the magnetic field.

In Simulink application, a Hall sensor is implemented as an array of logic blocks. The motor position information in degrees detected by the rotational motion sensor is supplied to an array of logic blocks. By performing *remainder after division* calculation between 360 degrees and the current position in degrees, the output remainder (between 0 and 360 degrees) is used to determine sector number information. The Hall sensor subsystem is shown in Figure 4.7.

At every time step, the rotor position is determined by Hall sensor in terms of sector number from 1 to 6. The corresponding logic block outputs the value of current sector number whereas the other logic block outputs zero. Note that the Hall effect sensor can be scaled to accommodate BLDC motors with more pole pairs. For  $n$  pole pairs, the position information of the rotor is multiplied by gain  $n$  to properly reflect the sector number. The BLDC motor in the thesis has 4 pole pairs.

#### 4.2.5 Commutation Logic

To run the motor continuously, switching patterns that provide instructions on how to commutate armature coils have to be supplied to the MOSFET switches in three-phase inverter. Commutation logic relies on sector number information provided by Hall sensor to select the corresponding switching pattern. It is a static table containing six switching patterns

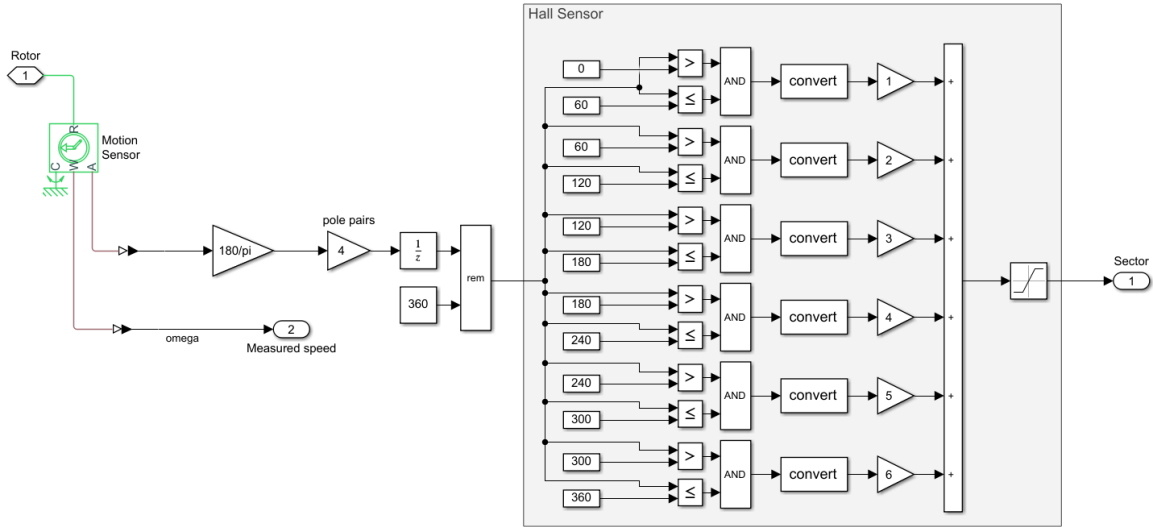


Figure 4.7: Block diagram for Hall effect sensor

each corresponding to an input sector number. The schematic view of a commutation table is shown in Figure 4.8.

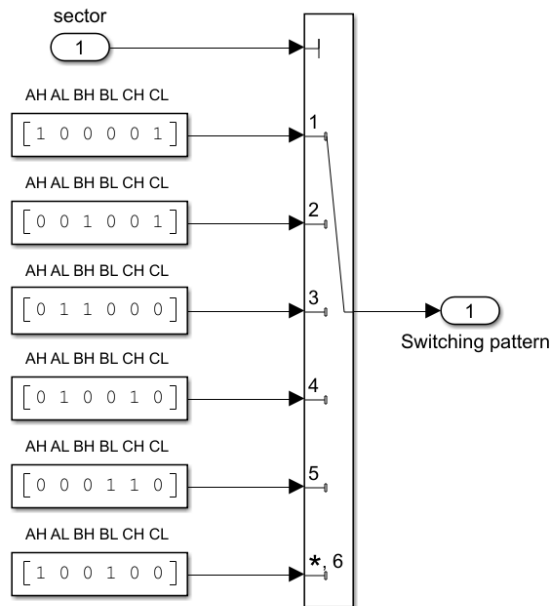


Figure 4.8: Commutation logic table

Every entry of the commutation table is a vector containing boolean values indicating on and off states for the six switches. For instance, if input sector number is 1, the vector [1 0 0 0 0 1] is active and instructs the three-phase inverter to energize coil A with positive

current and coil C with negative current, while coil B is not energized as both high and low switches for coil B are in off state.

The commutation logic subsystem completes the feedback loop for BLDC motor control. In summary, the closed loop contains the three-phase inverter with DC voltage source as the actuator, BLDC motor as the plant, Hall effect sensor to provide position feedback and commutation logic to issue command signal to the actuator. Note that a constant voltage source is only able to keep the motor spinning at a constant speed. Speed control under constant voltage input requires the implementation of PWM technique, which will be discussed in Section 4.2.6.

### 4.2.6 PWM Duty Cycle

The speed of a DC motor depends on the magnitude of the voltage applied to its armature coils. Two common methods to generate variable DC voltage is by either having a variable power supply or by switching the power supply on and off rapidly. Varying the power supply is not practical for automotive applications since the car battery is fixed at 14V. Modern DC motors are often controlled by power electronics systems which adjust the voltage by “chopping” the DC current into on and off cycles, known as pulse-width modulation (PWM). A PWM generating unit takes constant DC voltage as input and applies it to the motor with a series on and off states at high frequency, making the output voltage a square-waved shape. As a result, the motor is able to operate at an effective voltage between zero and full voltage to achieve variable speed.

To quantify the effective voltage output, the concept of PWM duty cycle is introduced. During each time period of PWM signal  $T_{\text{PWM}}$ , duty cycle is calculated as the percentage of “on” time  $T_{\text{on}}$  over PWM time period, as is represented in Equation 4.6:

$$\text{Duty Cycle} = \frac{T_{\text{on}}}{T_{\text{PWM}}} \times 100\% \quad (4.6)$$

Duty cycle is a fractional number between zero and one. The effective voltage output therefore equals to the product of duty cycle and source voltage as shown in Equation 4.7:

$$V_{\text{output}} = \text{Duty Cycle} \times V_{\text{source}} \quad (4.7)$$

The averaging effect of PWM duty cycle relies on the rate at which the power supply switches between on and off (switching frequency). Although it greatly depends on application, a higher switching frequency is preferred as it helps with closed-loop performance and stability for DC-DC inverter [50]. If the PWM switching frequency is too low, the motor

speed will exhibit ripple effect as it constantly tries to follow the square-wave shaped voltage supply, leading to poor tracking of reference speed. PWM switching frequency equals to the reciprocal of PWM time constant and it is shown in Equation 4.8:

$$f_{\text{PWM}} = \frac{1}{T_{\text{PWM}}} \quad (4.8)$$

The value of PWM time constant  $T_{\text{PWM}}$  should be significantly smaller than motor's time constant previously analyzed by Equation 4.5 in Section 4.2.1. The PWM time constant is chosen as  $T_{\text{PWM}} = 1 \times 10^{-4} \text{ s}$  as opposed to DC motor's time constant  $\tau = 0.0727 \text{ s}$ . As a result, PWM switching frequency  $f_{\text{PWM}}$  is equal to 10 kHz.

PWM duty cycle signal waves can be generated by modifying commutation logic subsystem. A second logic table with vector entries fully reversed (as opposed to the original table for every sector input) is added, along with a PWM generator block that generates unit pulse signal at PWM switching frequency. A threshold in the switch is set up so that it can switch between two logic tables at PWM switching frequency. The resulting block diagram for the modified commutation logic subsystem is shown in Figure 4.9.

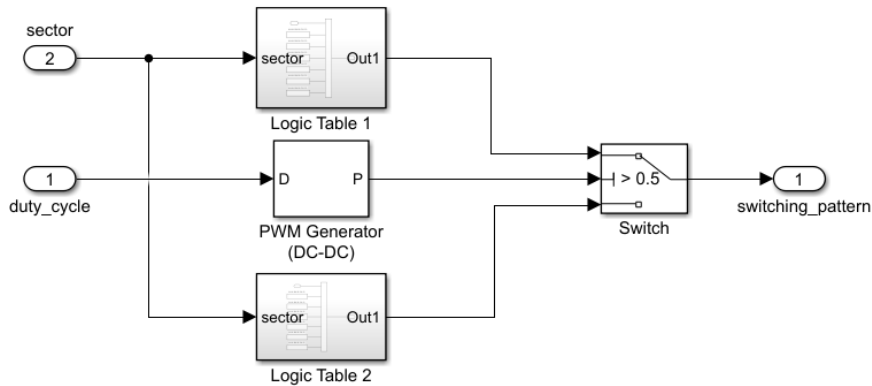


Figure 4.9: PWM generator with two logic tables and a switch

Signal waves to turn the 6 MOSFET switches on or off are shown in Figure 4.10. The six rows are corresponding to 6 MOSFET switches. As a result, during any sector number, the voltage flips between on and off at PWM frequency, resulting in an averaged voltage output on each coil. Another piece of information contained in Figure 4.10 is duty cycle, as can be roughly seen that “on” time’s portion over cycle time. The PWM duty cycle command input is generated by motor controller which will be discussed in Section 4.3.

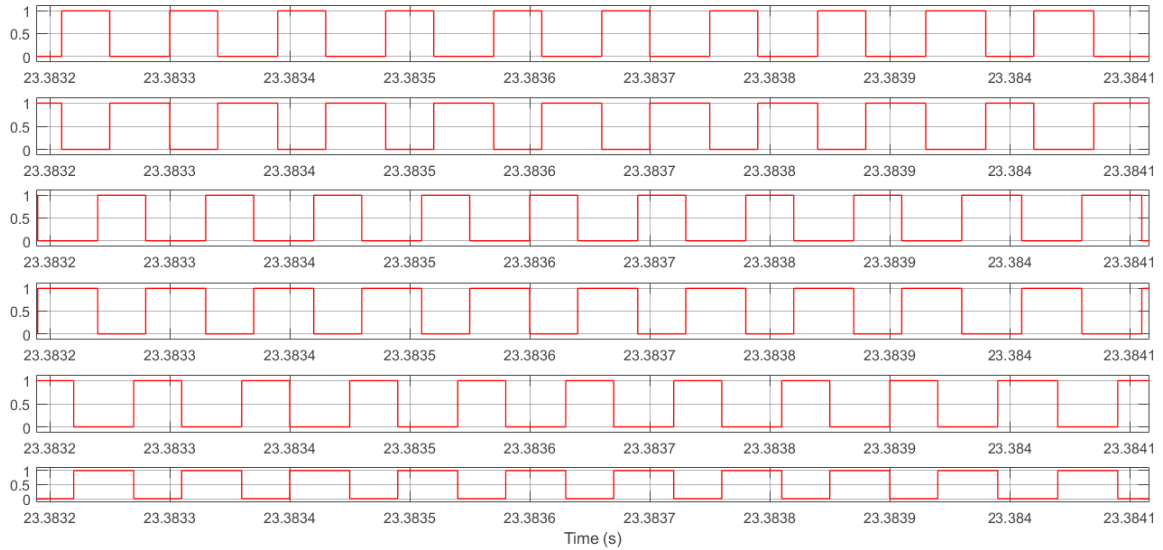


Figure 4.10: PWM duty cycle profile

#### 4.2.7 Blower Fan

The blower assembly is made up of a BLDC motor and an axial fan that is mounted on the same rotating shaft as the motor. Axial fans use a propeller to draw the air into the fan and discharge it in the same axial direction. Due to this configuration, the fan speed is the same as BLDC motor speed. The closed-loop control system of BLDC motor requires desired fan speed profile as reference input. Therefore, the steps used to derive fan speed profile are described below.

The fan speed profile as a function of air flow rate is plotted in Figure 4.11. The data points are acquired from literature [51]. The trend line is generated by Microsoft Excel using a second-order polynomial correlation. Comparing to other types of line fitting techniques, the error term  $R^2$  of the second-order polynomial correlation is close to 1, indicating a good fit of the line to the data.

The air flow is rated in standard cubic feet per minute (SCFM). It is the CFM at standard air density, defined as  $1.2 \text{ kg/m}^3$  or  $0.075 \text{ lb/ft}^3$ . The experimental data for air flow rate generated by the blower fan is available for High Ambient AUTO mode drive cycle test. By using the correlation equation, one can easily calculate required fan speed profile, as shown in Figure 4.12.

Note that the derived fan speed is in the range of the available data sets provided by the literature. Thus, it further validated the accuracy of the fan speed based derived from experimental air flow rate.

The fan model can be represented as a first-order linear equation, the same as an ideal

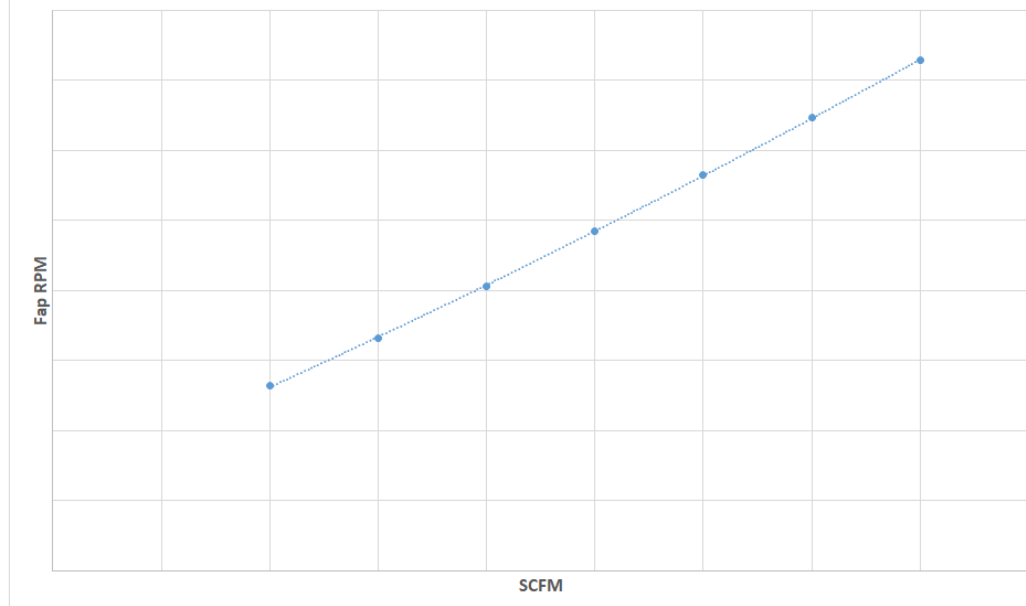


Figure 4.11: Fan speed (rpm) as a function of air flow rate (SCFM)

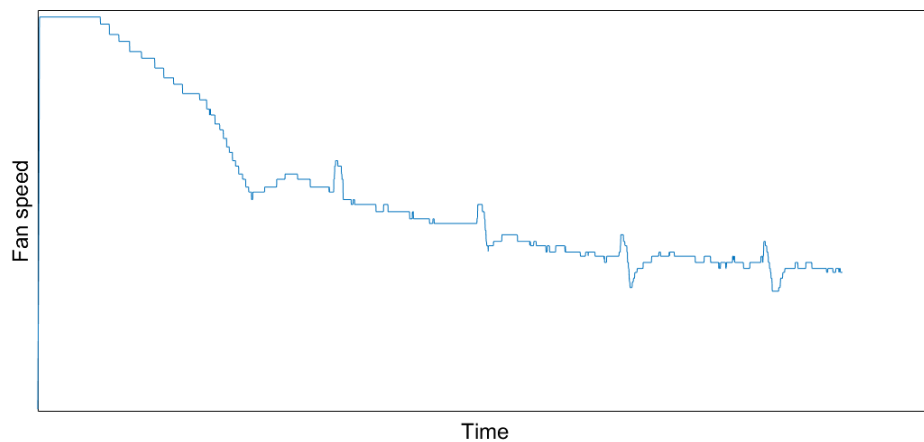


Figure 4.12: Derived fan speed profile for High Ambient AUTO mode drive cycle

rotational disk. In Equation 4.9,  $J$  is mass moment of inertia,  $b$  is frictional coefficient and input  $T_{in}(t)$  is the applied torque. Solving the first-order model will yield angular velocity  $\omega(t)$ .

$$J\dot{\omega} + b\omega = T_{in}(t) \quad (4.9)$$

In Simulink, the fan is considered as part of the BLDC motor with its moment of inertia and frictional coefficient merged into the properties of the motor. The actual output speed of the motor/fan is used as the error term for motor controller discussed in 4.3.

### 4.3 DC Motor Controller

The speed of BLDC motor and fan assembly at steady state is a constant value, due to a fixed 14V voltage source. To track the desired fan speed in order to provide optimal air flow rate, a speed controller is added to the closed-loop system to close the gap between reference speed and system's output speed by issuing PWM duty cycle signal to adjust effective voltage to the motor.

PID controllers are commonly seen in feedback control systems. It takes the feedback error signal  $E(s)$  as input and produces three control signals that are summed together to create control signal  $U(s)$  for the plant. In BLDC motor assembly, the output motor speed measured by sensor is fed back to the sum block to get the error term based on desired speed, and the controller's output is PWM duty cycle for regulating the voltage supply to BLDC motor's armature coils. PID controller's logic equation in Laplace domain is shown in Equation 4.10:

$$U(s) = K_P E(s) + K_I \frac{E(s)}{s} + K_D s E(s) \quad (4.10)$$

The three constants in front of the combined control signal are proportional gain  $K_P$ , integral gain  $K_I$  and derivative gain  $K_D$ . The proportional control signal is linearly proportional to the error term; increasing  $K_P$  tends to speed up the system response time. The integral term is related to the integral of past error signals; it ensures that the control signal will not be zero when the system is near steady state and therefore it is used to reduce tracking error. Lastly, the derivative term is used for adding damping and reducing overshoot to the closed-loop system.

Consider a closed-loop DC motor system with a PID type controller and a sensor shown in Figure 4.13.

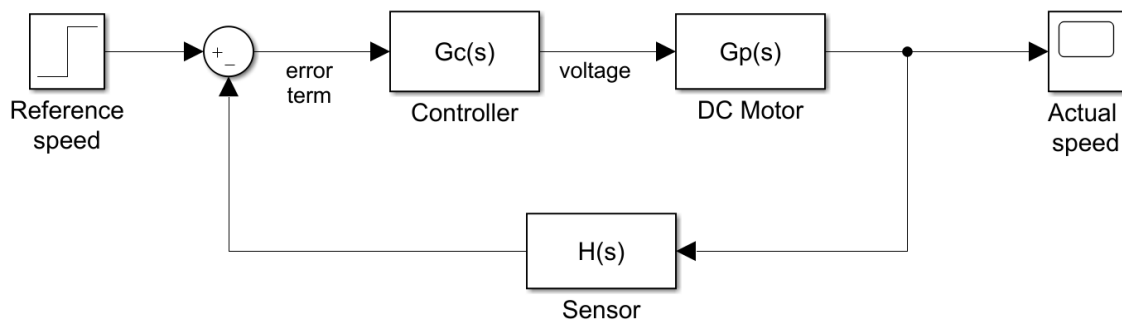


Figure 4.13: Closed-loop block diagram for DC motor control

Based on the linear system analysis in Section 4.2.1, transfer functions for PID controller, DC motor plant and the overall system transfer function are listed in Equation set 4.11:

$$G_C(s) = K_P + \frac{K_I}{s} + K_D s \quad (4.11a)$$

$$G_P(s) = \frac{K_m}{LJ s^2 + (Lb + RJ)s + (Rb + K_m K_b)} \quad (4.11b)$$

$$G(s) = \frac{G_C(s)G_P(s)}{1 + G_C(s)G_P(s)H(s)} \quad (4.11c)$$

To continue on the linear analysis, same set of parameters is applied to the DC motor (summarized in Table 4.1 in Section 4.2.1). The sensor is set to provide a unity feedback with  $H(s) = 1$ , effectively setting the maximum DC gain to 1. The reference speed is set to 3000 rpm. The first step is to analyze the effect of proportional gain to system's response and steady state output. The system's response with P controller at three different proportional gains are shown in Figure 4.14.

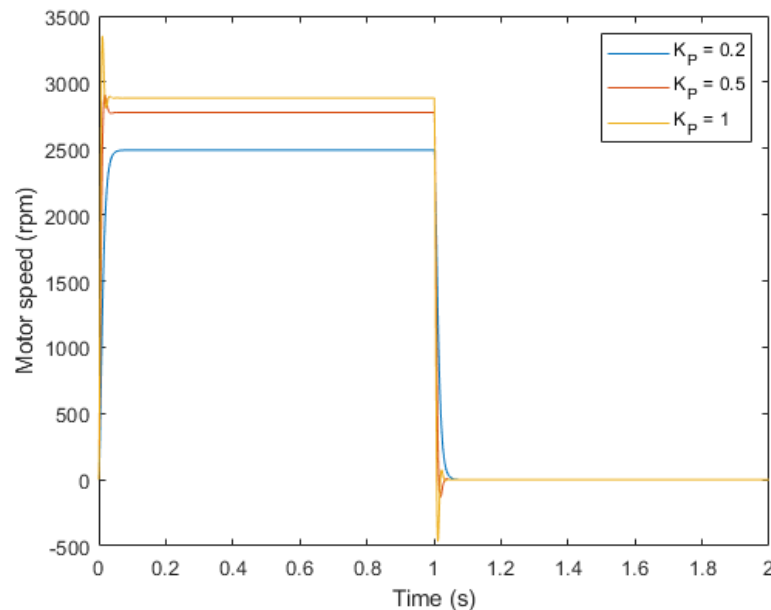


Figure 4.14: DC motor response with P controller

Increasing the proportional gain would reduce the time constant and settling time to reach steady state. On the other hand, a well damped system may experience oscillation with a large proportional gain.  $K_P$  at 0.2, 0.5 and 1 will produce DC gain of 0.8290, 0.9238 and 0.9604, respectively. However, DC gain never reaches unity as a reduced error term

would produce a zero command output. The steady state value will converge to but never reach the reference input. As a result, P controller alone is not able to provide steady-state tracking as a zero error term would result in a zero proportional term. Additionally, the motor cannot sustain at a constant speed with P controller if there are any input torque caused by load or friction.

Another important aspect to consider when applying a large  $K_P$  gain is the voltage requirement. Since gain  $K_P$  has unit  $V \cdot s/rad$ , at  $K_P = 1$  an error term of 314 rad/s (3000 rpm) when the motor starts from rest requires 314V power supply which is not feasible by a car battery.

Based on the result that a P controller alone cannot reduce the steady-state tracking error, PI controller can provide command signal even when the error term is zero during steady state. Figure 4.15 shows that any integral gain  $K_I$  is able to track reference speed perfectly with DC gain equal to unity.

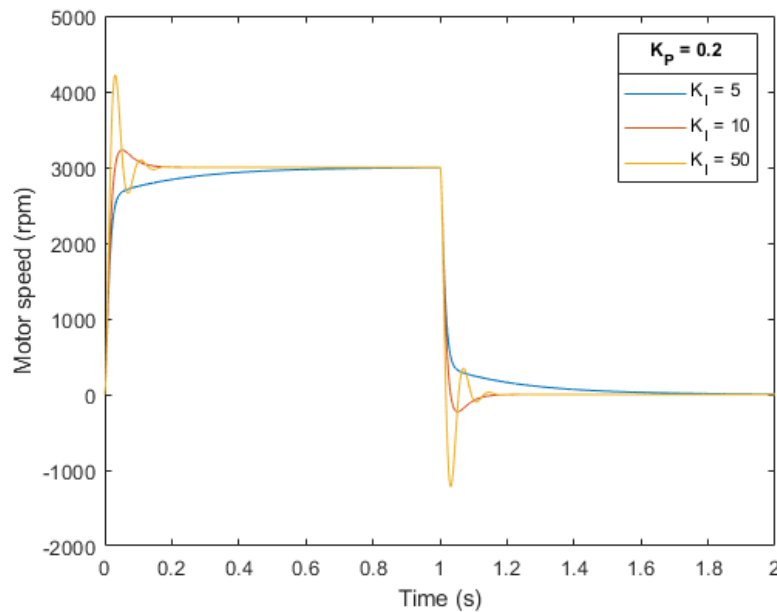


Figure 4.15: DC motor response with PI controller

Small integral gain  $K_I$  gives an over-damped system that reaches steady state rather slowly. As integral gain  $K_I$  increase, the system starts to show oscillation. In summary, PI controller is able to eliminate steady-state tracking error at the expense of slightly slower system response compared to P controller alone.

As previously analyzed in Section 4.2.1, the DC motor system shows sufficient damping and no oscillation. Therefore, the derivative term can be omitted by setting derivative gain  $K_D$  to zero.

### 4.3.1 Tuning Rules

Ziegler and Nichols [29] developed general tuning rules to select the gains for PID type controller. Based on heuristic experiments, these rules provide a good starting point for getting satisfactory closed-loop performance. However, each rules has its limitation and may not suit all types of systems. Further adjustments on the gains based on the target system are needed to improve transient response.

The *Ultimate Gain* Method relies on obtaining a marginally stable closed-loop response with a high proportional gain. The tuning rules are summarized in Table 4.3.

Table 4.3: Ziegler-Nichols: Ultimate Gain Method

Controller Type	Gains
P	$K_P = 0.5K_U$
PI	$K_P = 0.45K_U \quad K_I = \frac{0.54K_U}{P_U}$
PID	$K_P = 0.6K_U \quad K_I = \frac{1.2K_U}{P_U} \quad K_D = 0.075K_U P_U$

To apply this technique, first increase proportional gain  $K_P$  until closed-loop transient response goes from damped sinusoidal osculation to undamped oscillation with a constant amplitude. The time period of constant oscillation is called “ultimate period”  $P_U$ , which corresponds to the “ultimate gain”  $K_U$ . The integral and derivative gains are then calculated based on these two parameters.

The caveat of this technique is that system stability is sacrificed as the proportional gain is increased to a point in which the system is only marginally stable. Moreover, a high proportional gain may cause the actuator (DC motor in this case) not able to follow the control signal due to voltage supply limitation. As a result, the system’s transient response can never reach undamped oscillation despite a high value of gain  $K_P$ . Still, these general tuning rules provide a starting point for manually adjusting the gains to better understand the system.

Another set of tuning rules called *Reaction Curve* Method is also applied. Ziegler and Nichols claimed that many dynamic systems’ open-loop response to a step input is a damped S-shaped curve with no overshoot. Two parameters, namely the delay time  $T_d$  and the slope of the curve  $R$ , can be measured by drawing a tangent line to the S-shaped curve at the inflection point. The PID gains are then calculated based on the two parameters to produce a steady state output of approximately one quarter of its peak value in one time period of oscillation. The heuristic equations of *Reaction Curve* Method are summarized in Table 4.4.

Table 4.4: Ziegler-Nichols: Reaction Curve Method

Controller Type	Gains
P	$K_P = \frac{1}{RT_d}$
PI	$K_K = \frac{0.9}{RT_d}$ $K_I = \frac{0.27}{RT_d^2}$
PID	$K_P = \frac{1.2}{RT_d}$ $K_I = \frac{0.6}{RT_d^2}$ $K_D = \frac{0.6}{R}$

The two sets of PID tuning rules complement each other and provide insights into how to select a good baseline in terms of proportional and integral gains of DC motor controller. However, it should be emphasized that tuning rules have initial assumptions made towards the plant and desired output. Therefore, solely relying on tuning rules may not yield desirable results for all types of systems. Further tuning based on the actual plant is a requirement. The rules are merely serving as a starting point.

### 4.3.2 Discrete Time Domain

Digital controller design are implemented as software algorithms reside in computers. The signals are processed by microprocessors at a discrete time step specified by the user or determined by Simulink's numerical solver automatically. In the real world, physical systems carry out operations in a continuous-time domain. The signals of physical operations are converted to discrete-time domain for digital computers to be able to read and process.

The continuous-to-discrete (or analog-to-digital, A/D) conversion process involves sampling the continuous signal at a certain time step. The choice of sampling frequency depends on factors such as the time constant of physical system (i.e., the BLDC motor), desired level of accuracy and computational effort. In Simulink, time step can be set as fixed with user-specified value; or it can be set as variable and it's up to the numerical solver to determine the appropriate value by specifying desired level of accuracy.

In addition to global settings, it is possible to set local parameters for certain plant systems that may require different settings from the global system. For instance, the sampling frequency for BLDC motor can be set to relatively high since its time constant is small compared to other components in the closed-loop system. Ideally, local accuracy can be satisfied while computational effort is contained at a reasonable level for the system.

PID type controller can also adapt to discrete-time domain in order to be implemented as an algorithm in computers. Recall in Equation 4.10, the PI controller is designed in continuous-time domain with the error term  $E(s)$  and command signal  $U(s)$ . Once the

controller is tuned in continuous-time domain (s-domain), it must be converted to discrete-time domain (z-domain) with the knowledge of sampling time  $T_s$ . Numerical integral of the discrete error term leads to the integral part  $\frac{1}{z-1}$ , as shown in Equation 4.12:

$$G(z) = K_P + K_I \cdot T_s \frac{1}{z-1} \quad (4.12)$$

After the digital signals are processed by computers, the control signals issued by the controller are converted back to continuous-time domain to feed to the actuator. The discrete-to-continuous (or digital-to-analog, D/A) conversion is achieved by adding a *zero-order hold* block between controller and physical plant. The zero-order hold block converts discrete-time control signal to an continuous-time output signal. It does so by holding the digital value constant during the sample interval and only changing the output at the next sample interval when a new control signal is computed.

A more sophisticated implementation of zero-order hold is called *unit-delay*, which prevents any algebraic loop that may occur in the model. In Simulink, an algebraic loop occurs when there are only direct feed-through blocks exist within a loop, meaning that Simulink needs the value of the block's input signal to compute its output at the current time step. Such a signal loop creates a circular dependency of block outputs and inputs in the same time-step. This results in an algebraic equation that needs solving at each time-step, adding computational cost to the simulation.

### 4.3.3 Numerical Solver

The numerical results of simulations run on the same model can behave differently depending on solver settings. The goal of the simulation is to isolate all the solvers involved in each part of the system so that the most appropriate settings can be applied. The experimental data is taken at every second (sample rate is equal to 1 Hz) for the total duration of the drive cycle test. Solver selection must be chosen properly to represent the physical system.

There are two types of solvers to choose from: fixed-step and variable-step. Fixed-step solver uses user-defined step size throughout the simulation, whereas variable-step solver can adjust the step size automatically during the simulation. Solver type selection (fixed-step or variable-step) depends not only on the characteristics of the model, but also on the way the model will be deployed. For instance, real-time simulation requires fixed-step solver, as the variable-step size cannot be mapped to the real-time clock. Generally, variable-step solver is preferred to fixed-step solver, especially for systems in which dynamics appear and disappear locally. Hence, the step size is adjusted such that it gives desired level of accuracy in transient behaviour and reduces computing effort in steady state. In Simulink, the default

option is to use variable-step type solver.

For variable-step solver, it is possible to set up relative tolerance and to specify maximum and minimum step sizes. During each simulation run, Simulink calculates a time step based on an estimated error between the simulated solution and the actual solution. Reducing the solver relative tolerance does not always improve accuracy as the numerical solver will hit its limitation that depends on the particular model. The minimal accuracy required for the problem has to be estimated and choose the solver accordingly to minimize computational effort. Fortunately, for both Amesim and Simulink, the default value of  $1 \times 10^{-7}$  seems to be working correctly.

Besides step size, a solver can be discrete or continuous with respect to internal states of the model. Continuous solvers use numerical integration to compute a model's continuous state at current time step based on the state (and state derivatives) at a previous time step. Continuous solver must be chosen if there exist any continuous states in either Amesim. Since Amesim plant model contains only continuous states (called explicit state variables in Amesim), continuous solver is automatically loaded in Amesim. In Simulink, the choice is limited to discrete solver only.

For Simulink Simscape components, such as the brushless DC motor, local solvers can be applied to override global solver settings. This becomes helpful as the sample time of the experimental data is too large for accurate modelling of a DC motor. It is even possible to achieve multi-rate simulation with different physical components using their local solvers having different sample times. The solver updates the states once per time step; a component using a local solver appears to the global Simulink solver as if it has discrete states.

# Chapter 5

## Results and Discussion

The results of systems modelling and simulation are grouped into two parts: thermal systems performance is summarized in Section 5.1, controlled DC motor system's performance in Section 5.2. The results are presented separately due to the fact that they are modelled independently with distinct design approaches. Yet, they serve the same goal as to achieve a full virtual product development.

### 5.1 Thermal Systems Performance

Following the design steps outlined in Chapter 3, AC refrigerant loop is first built and calibrated against drive cycle experimental data. It is then attached to the cabin air model for fine tuning of thermal properties to achieve a combined vehicle thermal system. The performance of refrigerant loop alone is presented in Section 5.1.1; the performance of cabin air model in a combined thermal system is discussed in Section 5.1.2.

#### 5.1.1 A/C Refrigerant Loop

For the A/C refrigerant loop, the most important metric is the evaporator outlet air temperature, as it is going to be supplied to the cabin air model. The air side conditions such as temperature and air flow rate are taken directly from the experimental data as the baseline. The evaporator outlet air temperature depends on the conditions of the refrigerant fluid and the heat exchange over at the evaporator level. Therefore, the result effectively decides the cooling capacity of the A/C system. In Figure 5.1, evaporator outlet air temperatures are plotted for both simulation and experimental data for the entire duration of High Ambient AUTO mode drive cycle test. The simulation data is sampled every second to align with the experimental recordings.

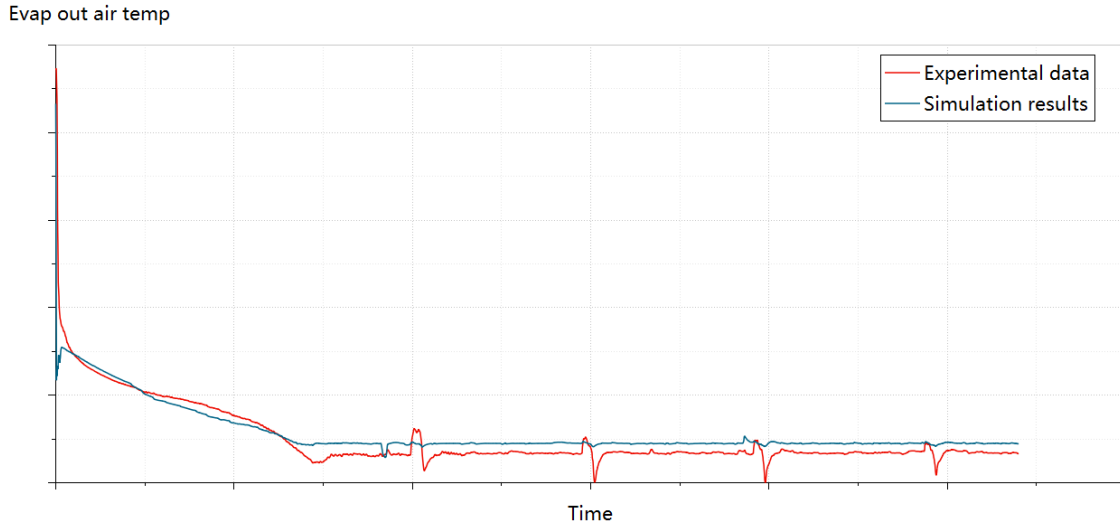


Figure 5.1: Evaporator outlet air temperate

The simulation results follow the general trend of experimental data reasonably well. The simulation temperature drops quickly during the initial stage of drive cycle, possibly due to a less-than-real thermal inertia presented in the virtual loop. For instance, the size of the IHX could be too small to provide enough damping. The other possibility is that initial condition exist in all the components and plays a vital part in the transient response; it is not be possible to specify initial condition for every component in Amesim. Therefore, the virtual system may start in an advantage compared to the real system.

Notice that the experimental data curve experienced fluctuations periodically during the drive cycle test, with temperature dipping to  $0^{\circ}\text{C}$  at certain time steps. This undesired behaviour can be due to engine speed fluctuations, as the vehicle accelerates from city driving speed to a higher speed. Gear shift may also bring disturbance to engine speed, which may affect compressor speed and eventually the performance of A/C refrigerant loop. Moreover, the temperature fluctuations could be due to the periodic air purging operation defined in the AUTO mode algorithm, as the re-circulation mode requires fresh air in-take to purge re-circulated cabin air. Since ambient air is much warmer than cabin air, it leaves the evaporator at a higher temperature as well. This explains the temperature spikes in a periodic manner.

Continue on with A/C refrigerant loop analysis. Temperature discrepancies exist at steady-state operation, with the simulated temperature slightly higher than the experimental data. It could be due to a number of factors in terms modelling inaccuracies. For instance, the velocity and temperature distribution map files used for modelling the condenser are not designed for High Ambient AUTO mode drive cycle speed profile; the values have to

be interpolated. As a result, condensers and potentially other heat exchangers, although calibrated, may still show deviations on heat rejection and pressure drop performances.

The compressor's discharge pressure at the discharge port is compared against experimental data, as shown in Figure 5.2.

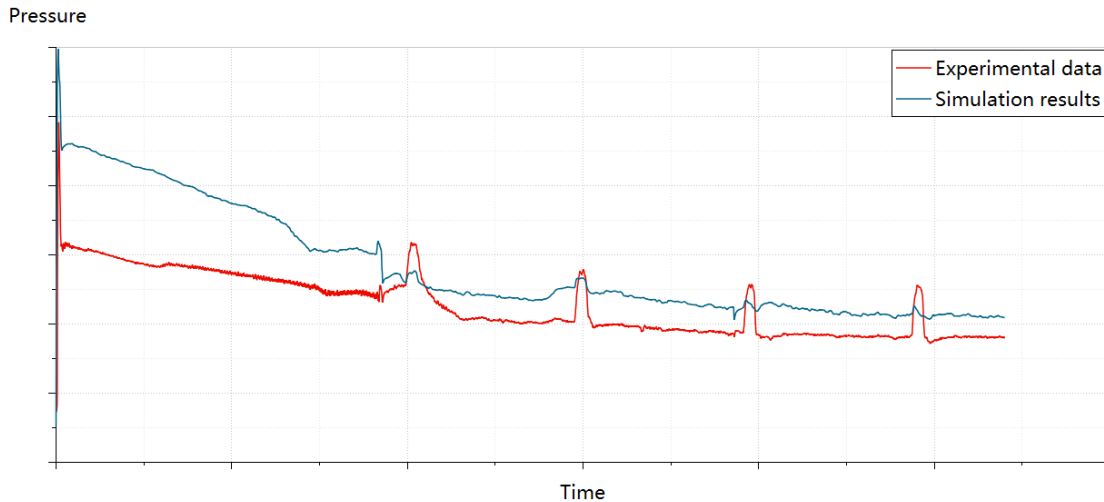


Figure 5.2: Compressor discharge pressure

The working state of the refrigerant does not impose direct influence on the cabin air model, rather, it serves as a way to perform quality check on whether the AC refrigerant loop is working as intended. The pressure deviation from the real system is anticipated, due to the fact that virtual A/C refrigerant loop cannot perfectly replicate various fluid frictions and losses happening along the real system. It may be improved by dialing down the efficiency parameters on the compressor and adding fluid frictions along the virtual loop.

### 5.1.2 Cabin Air Model

The cabin air model runs together with a calibrated A/C refrigerant loop. The heat load received by the cabin model is dissipated at the evaporator level by constant air re-circulation. The calibration process of cabin air model described in Section 3.3.4 involves adjusting the thermal mass and internal convective heat transfer coefficients so that the cabin air temperature curve follows the experimental results, as shown in Figure 5.3.

During the initial stage of drive cycle simulation, thermal mass configuration inside the cabin plays a vital part in the transient cool-down curve, as the thermal inertia introduced by thermal mass dictates how quickly the cabin temperature declines under the maximum performance of the refrigerant loop. As the system approaches steady state, other factors become more influential in regards to error tracking performance. External factors includ-

Cabin air temperature

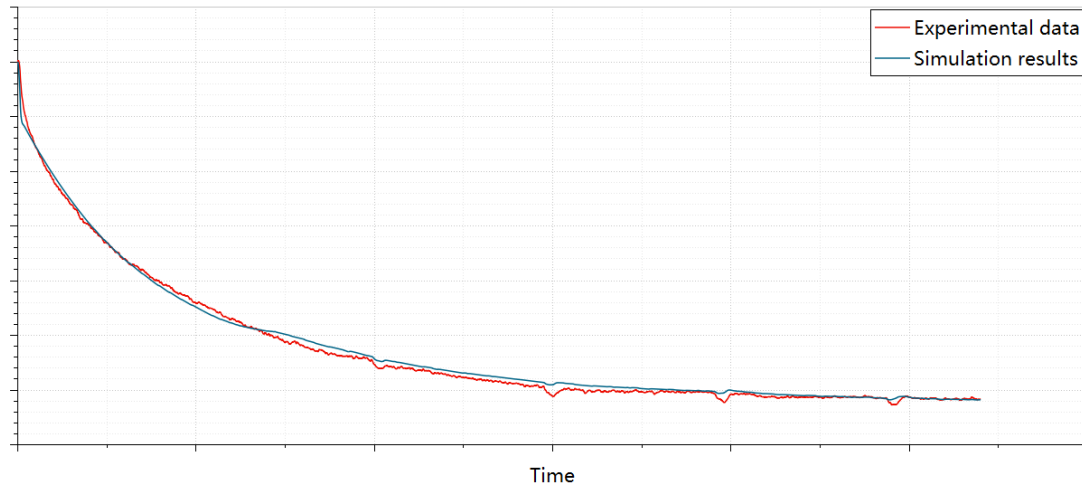


Figure 5.3: Cabin air temperate

ing A/C cooling load and solar heat load, internal factors such as glass properties, heat convection and conduction all play a part in the cabin air temperature curve.

There are non-ideal factors that may contribute unaccounted heat load to the cabin. These factors include but are not limited to: air leakages through door and window gaps, heat generated by dashboard electronics and blower motor. One of the most influential factor could be human flux model that simulates the heat and humidity generated by passengers. However, due to the fact that High Ambient AUTO mode drive cycle does not include human passengers, it is omitted in the virtual model.

## 5.2 DC Motor Performance

The design of feedback control system for DC motor follows a list of general performance requirements listed below:

- Response to reference: the controlled system must quickly respond to a new reference command.
- Damping characteristics: overshoot should be eliminated or contained reasonably small when the system output approaches the desired reference.
- Steady-state error: the tracking error should be minimized or eliminated as system reaches steady state.
- Disturbance attenuation or rejection: the system should be able to demonstrate adequate performance should disturbance inputs exist.

To evaluate the performance of controller design, the actual speed is compared against reference speed, shown in the top part of Figure 5.4. The bottom part of the Figure contains information on the command input of the PI controller in voltage over the first 30 seconds of simulation.

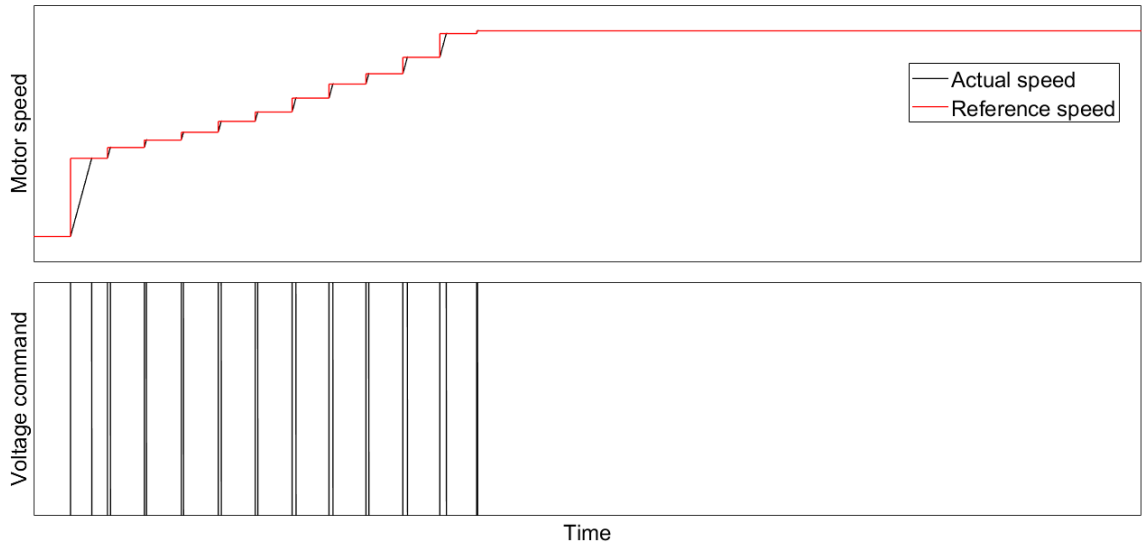


Figure 5.4: DC motor's speed tracking performance and controller's voltage command

It can be clearly seen that the actual motor speed tracks the reference speed very well in the entire operating range (from 0 to around 3000 rpm). Due to the fact that the reference speed is sampled at every second, the information on the transient response of the system is not preserved. Still, at the very least, the controlled system is able to react quickly (within 1 second) to the change of reference command. The overshoot is not visible at this time step setting.

The PI controller's command voltage information is shown in the bottom half of Figure 5.4. The command peaks at 14V to accelerate the DC motor. Once the speed matches the reference, the command drops to a value just above zero to maintain its speed.

It should be noted that the sampling frequency of the two parts are different: the controller is sampled at a much smaller time step in Simulink (same as the BLDC motor's time constant), while the reference signal is in a "stair-step" shape due to the low sampling frequency of the experimental data. The reference signal's value is constant during each one-second sampling time. The BLDC motor's actual speed is able to track the "stair-step" due to the fact that the settling time  $t_s = 4\tau_2 = 0.2909$  s, based on the linear analysis.

The overall simulation result is shown in Figure 5.5. In order to run the simulation for the entire drive cycle, computational size grows enormously to a point where it is not possible to run on the author's computer. Therefore, a compromise is made such that the

simulation is scaled down by treating 1 second of simulation time as 100 seconds in real time. In other words, the reference speed signal is sampled at every hundred seconds so that for instance, a 1000-second experiment can be represented by a 10-second simulation.

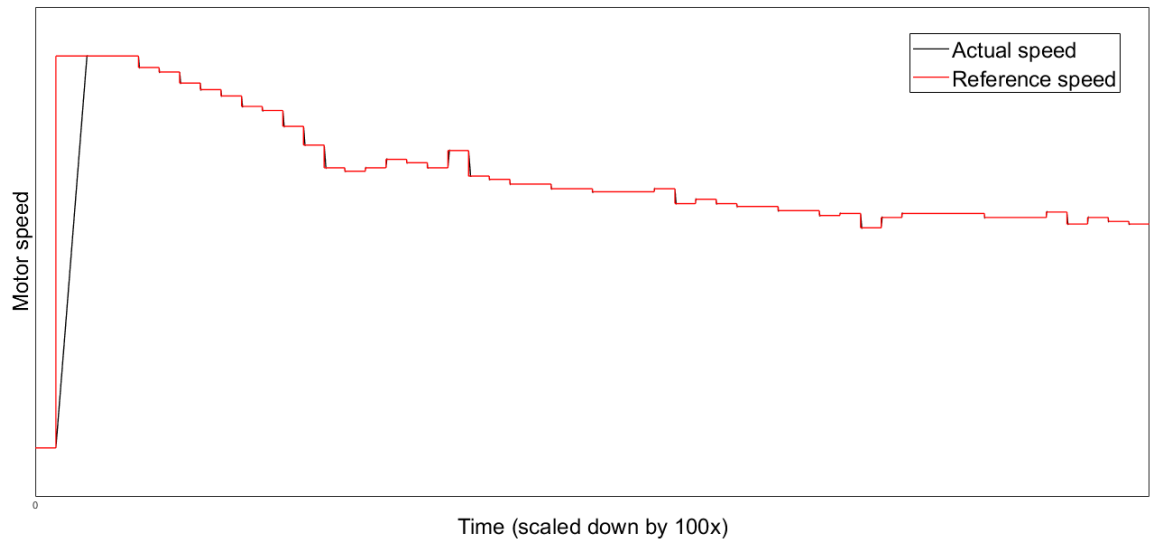


Figure 5.5: DC motor’s speed and reference speed (scaled down by 100x)

The explanation is that the controlled system is able to track reference speed in an “accelerated mode” even at a 100x real time. Note that the result for the actual speed at the first time step provides no meaningful information as the real time is at 100 seconds. For the system’s actual performance over the first 30 seconds, refer to the top part of Figure 5.4. Overall, the results prove that the controlled system is able to track reference speed over the entire working range of High Ambient AUTO mode drive cycle with good response time and no overshoot.

# Chapter 6

## Conclusion and Future Work

It has been demonstrated in Chapter 3 and Chapter 4 that the A/C system, including the refrigerant loop, cabin air model and blower assembly on the vehicle can be modelled virtually through 1D approach. The performances of each virtual thermal model are validated against experimental data and show good alignment. The combined refrigerant loop and cabin air model is able to fully simulate the cabin air temperature development during High Ambient AUTO mode drive cycle. the DC motor model is able to track reference speed to generate adequate air flow rate for the cabin. Overall, the major objectives listed under Section 1.2 are met, along with deeper understandings on thermal and control systems design.

The virtual A/C model can be used to generate detailed A/C system performance for component analysis and optimization. For High Ambient AUTO mode drive cycle, software simulation based on the virtual model can be used in place of physical test conducted in climate chamber. Moreover, if minor modifications, such as a component swap, are made to the system, the updated performance results can be obtained directly from the virtual model without conducting physical experiments. As a result, product development pace is accelerated and the cost is reduced.

In principle, the virtual model can also be adapted to drive cycle profiles other than High Ambient AUTO mode drive cycle with minimum adjustment needed. Preparation work include re-initializing the refrigerant charge in the A/C loop and re-calibrating the thermal properties of the cabin model. Ultimately, the virtual model serves as a powerful yet flexible platform for A/C system development.

### 6.1 Future Work

Based on the outcome of the thesis, there are still room for further research and improvement. The most anticipated feature by the author is the integration of the blower assembly

into vehicle thermal model. Currently, the blower fan air flow rate recorded in the experimental test is used to generate reference fan speed for the DC motor controller, as well as to provide the boundary condition for the thermal systems. The blower assembly is a standalone MATLAB/Simulink project while the thermal systems are implemented in Amesim. The two systems operate in different domains and are independent of each other.

In an integrated scheme, the combined refrigerant loop and cabin air model essentially become a plant of the controlled DC motor system. The DC motor controller is able to adjust the fan speed based on the knowledge of cabin air temperature computed by Amesim. For the controller design, there lies the opportunity to explore different control algorithms such as model predictive control and fuzzy logic control, both of which are reviewed in Chapter 2 but have not been implemented in this thesis.

To co-simulate thermal model and control system between Amesim and Simulink, it is necessary to adjust the compiler settings in both software so that compiled model files can be used interchangeably. The detailed instructions on how to prepare the models for co-simulation is provided by Amesim User's Guide [2].

# Bibliography

- [1] Refrigeration Compressors and Air Conditioning Compressors Information. URL [https://www.globalspec.com/learnmore/building\\_construction/hvac/ventilation/refrigeration\\_compressors\\_air\\_conditioning\\_compressors/](https://www.globalspec.com/learnmore/building_construction/hvac/ventilation/refrigeration_compressors_air_conditioning_compressors/).
- [2] Simcenter Amesim 17 for Windows. URL <https://www.plm.automation.siemens.com/global/en/products/simcenter/simcenter-amesim.html/>.
- [3] Introduction to Brushless DC Motor Control. URL <https://explore.mathworks.com/brushless-dc-motors-introduction/>.
- [4] S. Natarajan, S. K. S, R. Amaral, and S. Rahman. 1D Modeling of AC Refrigerant Loop and Vehicle Cabin to Simulate Soak and Cool Down. In *SAE 2013 World Congress & Exhibition*. SAE International. doi: 10.4271/2013-01-1502. URL <https://doi.org/10.4271/2013-01-1502/>.
- [5] T. Kiss and J. Lustbader. Comparison of the Accuracy and Speed of Transient Mobile A/C System Simulation Models. 7(2):739–754. ISSN 1946-4002. doi: 10.4271/2014-01-0669. URL <https://www.sae.org/content/2014-01-0669/>.
- [6] T. Ye. A Multidisciplinary Numerical Modeling Tool Integrating CFD and Thermal System Simulation for Automotive HVAC System Design. In *SAE 2012 World Congress & Exhibition*. SAE International. doi: 10.4271/2012-01-0644. URL <https://doi.org/10.4271/2012-01-0644/>.
- [7] K. Bhambare, J. Fukuyama, J. Han, K. Masuzawa, A. Iwanaga, and S. Patterson. Three Dimensional Transient Analysis of the Climate Inside a Passenger Vehicle Cabin under Solar Load. pages 2014–01–0702. doi: 10.4271/2014-01-0702. URL <https://www.sae.org/content/2014-01-0702/>.
- [8] R. Pathuri, Y. Patil, and P. V. Nagarhalli. Deployment of 1D Simulation with Multi Air Zone Cabin Model for Air Conditioning System Development for Passenger Car.

- pages 2015–26–0234. doi: 10.4271/2015-26-0234. URL <https://www.sae.org/content/2015-26-0234/>.
- [9] G. Peri, S. Sambandan, and S. Sathish Kumar. Cool Down Analysis of an HVAC System Using Multi-Zone Cabin Approach. pages 2017–01–0182. doi: 10.4271/2017-01-0182. URL <https://www.sae.org/content/2017-01-0182/>.
- [10] V. Muthusamy, S. Sathish Kumar, and S. Sambandan. Investigation of a Dual HVAC MAC System with Three Row Ducts Using 1D Modeling. pages 2017–01–0164. doi: 10.4271/2017-01-0164. URL <https://www.sae.org/content/2017-01-0164/>.
- [11] E. Andrès, T. Gillet, R. Rullière, P. Haberschill, V. Lemort, G. Olivier, and A. El Bakkali. Modelling of an automotive multi-evaporator air-conditioning system. URL <https://docs.lib.purdue.edu/iracc/1639/>.
- [12] Y. Zheng, B. Mark, and H. Youmans. A Simple Method to Calculate Vehicle Heat Load. doi: 10.4271/2011-01-0127. URL <http://papers.sae.org/2011-01-0127/>.
- [13] M. A. Fayazbakhsh and M. Bahrami. Comprehensive Modeling of Vehicle Air Conditioning Loads Using Heat Balance Method. doi: 10.4271/2013-01-1507. URL <http://papers.sae.org/2013-01-1507/>.
- [14] S. Sanaye and M. Dehghandokht. Thermal Modeling for Predication of Automobile Cabin Air Temperature. 1(3):152–164. URL <http://www.iust.ac.ir/ijae/article-1-21-en.html/>.
- [15] J. Rugh, L. Chaney, L. Ramroth, T. Venson, and M. Rose. Impact of Solar Control PVB Glass on Vehicle Interior Temperatures, Air-Conditioning Capacity, Fuel Consumption, and Vehicle Range. doi: 10.4271/2013-01-0553. URL <http://papers.sae.org/2013-01-0553/>.
- [16] M. Simion, L. Socaciu, and P. Unguresan. Factors which Influence the Thermal Comfort Inside of Vehicles. 85:472–480. ISSN 18766102. doi: 10.1016/j.egypro.2015.12.229. URL <https://linkinghub.elsevier.com/retrieve/pii/S1876610215028945/>.
- [17] P. O. FANGER. *Thermal Comfort. Analysis and Applications in Environmental Engineering*. Copenhagen: Danish Technical Press. URL <https://www.cabdirect.org/cabdirect/abstract/19722700268/>.

- [18] D. Fiala. Dynamic simulation of human heat transfer and thermal comfort. URL <https://www.semanticscholar.org/paper/Dynamic-simulation-of-human-heat-transfer-and-Fiala/>.
- [19] M. Lorenz, D. Fiala, M. Spinnler, and T. Sattelmayer. A Coupled Numerical Model to Predict Heat Transfer and Passenger Thermal Comfort in Vehicle Cabins. In *SAE 2014 World Congress & Exhibition*. SAE International. doi: 10.4271/2014-01-0664. URL <https://doi.org/10.4271/2014-01-0664/>.
- [20] T. Kubota, T. Ishikawa, J. Tosaka, and H. Okayasu. Automotive Thermal Environment Model to Design Climate Control Logics Based on Thermal Sensation. In *WCX World Congress Experience*. SAE International. doi: 10.4271/2018-01-0064. URL <https://doi.org/10.4271/2018-01-0064/>.
- [21] A. Kelman and F. Borrelli. Bilinear Model Predictive Control of a HVAC System Using Sequential Quadratic Programming. 44(1):9869–9874. ISSN 14746670. doi: 10.3182/20110828-6-IT-1002.03811. URL <https://linkinghub.elsevier.com/retrieve/pii/S1474667016451979/>.
- [22] L.-X. Wang and J. Mendel. Generating fuzzy rules by learning from examples. 22(6):1414–1427, Nov.-Dec./1992. ISSN 00189472. doi: 10.1109/21.199466. URL <http://ieeexplore.ieee.org/document/199466/>.
- [23] T. Söderström and P. Stoica. *System Identification*. Prentice Hall International Series in Systems and Control Engineering. Prentice Hall. ISBN 978-0-13-881236-2. Includes indexes.
- [24] H. A. Nielsen and H. Madsen. Modelling the heat consumption in district heating systems using a grey-box approach. 38(1):63–71. ISSN 03787788. doi: 10.1016/j.enbuild.2005.05.002. URL <https://linkinghub.elsevier.com/retrieve/pii/S0378778805000745/>.
- [25] J. Sjöberg, Q. Zhang, L. Ljung, A. Benveniste, B. Deylon, P.-Y. Glorennec, H. Hjalmarsson, and A. Juditsky. Nonlinear Black-box Modeling in System Identification: A Unified Overview. ISSN 1400-3902.
- [26] R. Romijn, L. Özkan, S. Weiland, J. Ludlage, and W. Marquardt. A grey-box modeling approach for the reduction of nonlinear systems. 18(9):906–914. ISSN 09591524. doi: 10.1016/j.jprocont.2008.06.007. URL <https://linkinghub.elsevier.com/retrieve/pii/S0959152408001121/>.

- [27] J.-L. Lin and T.-J. Yeh. Modeling, identification and control of air-conditioning systems. 30(2):209–220. ISSN 01407007. doi: 10.1016/j.ijrefrig.2006.08.009. URL <https://linkinghub.elsevier.com/retrieve/pii/S0140700706001836/>.
- [28] H. O. Bansal, R. Sharma, and P. Shreeraman. PID controller tuning techniques: A review. 2(4):168–176.
- [29] J. G. Ziegler and N. B. Nichols. Optimum settings for automatic controllers. 64(11).
- [30] Y. Li, K. H. Ang, and G. C. Chong. PID Control System Analysis and Design. 26(1): 32–41. URL <https://ieeexplore.ieee.org/abstract/document/1580152/>.
- [31] C. Bohn and D. P. Atherton. An analysis package comparing PID anti-windup strategies. 15(2):34–40. ISSN 1941-000X. doi: 10.1109/37.375281.
- [32] A. Scottedward Hodel and C. Hall. Variable-structure PID control to prevent integrator windup. 48(2):442–451. ISSN 02780046. doi: 10.1109/41.915424. URL <http://ieeexplore.ieee.org/document/915424/>.
- [33] A. Visioli. A new design for a PID plus feedforward controller. 14(4):457–463. ISSN 09591524. doi: 10.1016/j.jprocont.2003.09.003. URL <https://linkinghub.elsevier.com/retrieve/pii/S0959152403000982/>.
- [34] I. Mizumoto, D. Ikeda, T. Hirahata, and Z. Iwai. Design of discrete time adaptive PID control systems with parallel feedforward compensator. 18(2):168–176. ISSN 09670661. doi: 10.1016/j.conengprac.2009.09.003. URL <https://linkinghub.elsevier.com/retrieve/pii/S0967066109001580/>.
- [35] T.-J. Yeh, Y.-J. Chen, W.-Y. Hwang, and J.-L. Lin. Incorporating fan control into air-conditioning systems to improve energy efficiency and transient response. 29(10): 1955–1964. ISSN 13594311. doi: 10.1016/j.applthermaleng.2008.09.017. URL <https://linkinghub.elsevier.com/retrieve/pii/S1359431108003839/>.
- [36] K. Mařík, J. Rojíček, P. Stluka, and J. Vass. Advanced HVAC Control: Theory vs. Reality. 44(1):3108–3113. ISSN 14746670. doi: 10.3182/20110828-6-IT-1002.03085. URL <https://linkinghub.elsevier.com/retrieve/pii/S1474667016440887/>.
- [37] T. H. Lim, Y. Shin, S. Kim, and C. Kwon. Predictive control of car refrigeration cycle with an electric compressor. 127:1223–1232. ISSN 13594311. doi: 10.

- 1016/j.applthermaleng.2017.08.125. URL <https://linkinghub.elsevier.com/retrieve/pii/S1359431116327697/>.
- [38] H. Wang, I. Kolmanovsky, M. R. Amini, and J. Sun. Model Predictive Climate Control of Connected and Automated Vehicles for Improved Energy Efficiency. In *2018 Annual American Control Conference (ACC)*, pages 828–833. IEEE. ISBN 978-1-5386-5428-6. doi: 10.23919/ACC.2018.8431051. URL <https://ieeexplore.ieee.org/document/8431051/>.
- [39] T. Kiss, L. Chaney, and J. Meyer. A New Automotive Air Conditioning System Simulation Tool Developed in MATLAB/Simulink. 6(2):826–840. ISSN 1946-4002. doi: 10.4271/2013-01-0850. URL <https://www.sae.org/content/2013-01-0850/>.
- [40] K. L. Ku, J. S. Liaw, M. Y. Tsai, and T. S. Liu. Automatic Control System for Thermal Comfort Based on Predicted Mean Vote and Energy Saving. 12(1):378–383. ISSN 1545-5955, 1558-3783. doi: 10.1109/TASE.2014.2366206. URL <http://ieeexplore.ieee.org/document/6963509/>.
- [41] S. Soyguder, M. Karakose, and H. Alli. Design and simulation of self-tuning PID-type fuzzy adaptive control for an expert HVAC system. 36(3):4566–4573. ISSN 09574174. doi: 10.1016/j.eswa.2008.05.031. URL <https://linkinghub.elsevier.com/retrieve/pii/S0957417408002200/>.
- [42] Y. Farzaneh and A. A. Tootoonchi. Controlling automobile thermal comfort using optimized fuzzy controller. 28(14-15):1906–1917. ISSN 13594311. doi: 10.1016/j.applthermaleng.2007.12.025. URL <https://linkinghub.elsevier.com/retrieve/pii/S1359431108000422/>.
- [43] B. Ibrahim, M. Aziah, S. Ahmad, R. Akmeliawati, H. Nizam, A. Muthalif, S. Toha, and M. Hassan. Fuzzy-based Temperature and Humidity Control for HV AC of Electric Vehicle. 41:904–910. ISSN 18777058. doi: 10.1016/j.proeng.2012.07.261. URL <https://linkinghub.elsevier.com/retrieve/pii/S1877705812026616/>.
- [44] J. M. Calm. The next generation of refrigerants – Historical review, considerations, and outlook. 31(7):1123–1133. ISSN 01407007. doi: 10.1016/j.ijrefrig.2008.01.013. URL <https://linkinghub.elsevier.com/retrieve/pii/S0140700708000261/>.
- [45] C. Li, E. Brewer, L. Pham, and H. Jung. Reducing Mobile Air Conditioner (MAC) Power Consumption Using Active Cabin-Air-Recirculation in A Plug-In Hybrid Elec-

- tric Vehicle (PHEV). 9(4):51. ISSN 2032-6653. doi: 10.3390/wevj9040051. URL <http://www.mdpi.com/2032-6653/9/4/51/>.
- [46] R. Bonnet. Calibration of heat exchanger in AC application: Explanation and example.
- [47] C. A. Kluever. *Dynamic Systems: Modeling, Simulation, and Control*. John Wiley and Sons, Inc. ISBN 978-1-118-28945-7.
- [48] MATLAB Primer. URL [https://www.mathworks.com/help/pdf\\_doc/matlab/learn\\_matlab.pdf](https://www.mathworks.com/help/pdf_doc/matlab/learn_matlab.pdf).
- [49] M. Taghizadeh, A. Ghaffari, and F. Najafi. Modeling and identification of a solenoid valve for PWM control applications. 337(3):131–140. ISSN 16310721. doi: 10.1016/j.crme.2009.03.009. URL <https://linkinghub.elsevier.com/retrieve/pii/S1631072109000308/>.
- [50] B. Lehman and R. Bass. Switching frequency dependent averaged models for PWM DC-DC converters. 11(1):89–98. ISSN 0885-8993, 1941-0107. doi: 10.1109/63.484421. URL <https://ieeexplore.ieee.org/document/484421/>.
- [51] Series LM & LMF Cast Aluminum Volume Blowers. URL [https://www.cincinnati.com/catalogs/LM\\_LMF-702-internet.pdf](https://www.cincinnati.com/catalogs/LM_LMF-702-internet.pdf).

# Appendix

## .1 MATLAB scripts for linear system analysis

```
close all
clear all
clc

L = 1.5e-3; % H
R = 0.5; % ohm
Km = 0.04; % Nm/A
Kb = Km; % V-s/rad
J = 2.5e-4; %kg-m2
b = 1e-4; % Nm-s/rad

sysArmature = tf(1,[L R]);
sysRotor = tf(1,[J b]);
sysG_AR = Km*sysArmature*sysRotor;
sysH_Kb = Kb;
sysT_DCmotor= feedback(sysG_AR,sysH_Kb)

%PI Controller

KP = 0.2; % V-s/rad
KI1= 1; % V/rad
KI2= 5;
KI3= 20;

s=tf('s');
sysG_c1 = KP + KI1/s;
```

```

sysG_c2 = KP + KI2/s;
sysG_c3 = KP + KI3/s;

sysG_p = sysT_DCmotor

sysG1 = sysG_c1*sysG_p;
sysG2 = sysG_c2*sysG_p;
sysG3 = sysG_c3*sysG_p;

sysH = 1; % 1

sysT1 = feedback(sysG1,sysH);
sysT2 = feedback(sysG2,sysH);
sysT3 = feedback(sysG3,sysH);

% Dynamic analysis
DCgain1 = dcgain(sysT1)
DCgain2 = dcgain(sysT2)
DCgain3 = dcgain(sysT3)

% Poles = pole(sysT)
% Tau1 = - 1/Poles(1);
% Tau2 = - 1/Poles(2);
% T_s = max(Tau1,Tau2)*4 % settling time

% Step response to input u
t = 0:0.001:2;
u = zeros(size(t));
u(1:1001) = 3000*2*pi/60; % define u=3000rpm for 0 <= t <= 1 s
[y1,t]=lsim(sysT1,u,t);
[y2,t]=lsim(sysT2,u,t);
[y3,t]=lsim(sysT3,u,t);
y1_rpm = y1*60/2/pi;
y2_rpm = y2*60/2/pi;
y3_rpm = y3*60/2/pi;

```

```
figure
plot(t,y1_rpm)
hold on
plot(t,y2_rpm)
hold on
plot(t,y3_rpm)
hold off
%title('Motor speed vs. Voltage')
xlabel('time (s)')
ylabel('rpm')
legend('K_I = 5', 'K_I = 10', 'K_I = 50')
```

# Vita Auctoris

NAME: Mingzhe Chang

PLACE OF BIRTH: Zhengzhou, China

YEAR OF BIRTH: 1994

EDUCATION: Columbia International College  
Hamilton, ON, 2013

University of Windsor, B.Sc.  
Windsor, ON, 2018

University of Windsor, M.Sc.  
Windsor, ON, 2020

Politecnico di Torino, M.Sc.  
Torino, Italy, 2020